Doctoral dissertation

Development of the Median Tectonic Line fault zone, Mie Prefecture, southwest Japan: Strain localization and softening

(西南日本、三重県の中央構造線断層帯の発展：歪の局所化と軟化)

Bui Van Dong

ブイ ヴァン ドン

Department of Natural History Sciences, Graduate School of Science,
Hokkaido University

3/2019

Abstract

The Median Tectonic Line (MTL) fault zone in Japan includes fault rocks that formed at different conditions of deformation. I examined the development of the MTL fault zone in Mie prefecture, central Japan, which originated from the Cretaceous Ryoke granitic rocks, in order to understand the development of fault rocks and architecture during exhumation. In the study area, the mylonitic rocks consist of two types of mylonitic rocks distributed in different areas at the north of the MTL. Area A mostly consists of protomylonite, which is up to c. 300 m wide from the MTL originated from tonalite and Area B which is up to c. 500 m wide and distributed further north, consists of mylonite which originated from granite. I use microstructures and crystallographic preferred orientations (CPOs) of quartz and microstructures of K-feldspar to constrain the deformation conditions and mechanisms and analyze a spatio-temporal distribution of these in the MTL fault zone along the Akaiwadani-River, western Mie prefecture.

Based on observed microstructures of quartz, it has been found that in Area B the mylonites consisting of recrystallized quartz grains with S-type microstructure created by subgrain rotation (SGR) recrystallization are distributed from the distance of 300 m to 490 m from the MTL, while those with P-type microstructure created by grain boundary migration (GMB) recrystallization are distributed from the distance of 490 m to 800 m from the MTL. In direct proximity to the MTL, Area A, protomylonite occurs, where recrystallized quartz grains are formed by SGR. The quartz c-axis CPOs dominantly show Y-maxima patterns in both areas A and B, however, some samples from the proto-mylonite in Area A show a type-I crossed girdle quartz c-axis fabric with R-maxima, and some of the S-type mylonites in Area B show a transitional quartz c-axis fabric between a Y-maximum and type-I crossed girdles. K-feldspar is abundant and strongly deformed in mylonite of Area B with intergrowth of myrmekite. K-feldspar microstructure shows brittle deformation in S-type mylonite, whereas, in P-type mylonite, K-feldspar porphyroclasts show ductile deformation with an elongated ribbon or fish shape.

The deformation of quartz occurred at high temperatures around 500 ^{o}C in the wide zone forming P-type quartz microstructures and large recrystallized grain size (c. 100 μm) in Area B, which is inferred from two-feldspar geothermometry. However, the strain became localized during cooling of the granitic mylonites in the southern part of Area B, where S-type microstructures and smaller recrystallized grains of quartz (c. 20 μm) formed. Ductile deformation of quartz to form S-type microstructures is inferred to

have occurred at 350 to 400 °C, based on two feldspar geothermometry. The strain localization occurred at differential stress of ~100 MPa and strain rate of 10^{-16} s^{-1} at temperature conditions of c. 400 °C, which is inferred from the experimentally determined constitutive equation of quartz flow law. Below 350 °C, ductile deformation stopped in mylonites in Area B and only occurred in a very narrow zone up to 50 m wide forming ultramylonite in direct proximity to the MTL (the southernmost part of area A). This strain localization might have been caused by water weakening in quartz following incorporation of fluids into the present MTL locality.

Acknowledgements

First, I would like to express my sincere gratitude to Professor Toru Takeshita for his support and supervision during my Ph.D. course.

Next, I am grateful to Professor Takaya Nagai, Associate Professor Jun Kameda (Hokkaido University), and Professor Ando (Hiroshima University) for discussion and helpful reviews.

In addition, I would like to send my great thank to Professor Junichi Ando (Hiroshima University) and Doctor Takafumi Yamamoto (Kobelco Research Institute) who taught and supported helpful techniques of TEM and EBSD, as well as give me a lot of advice.

I am also grateful to Doctor Akiko Matsumoto (Hokkaido University) for helpful technical supporting of EBSD and EPMA.

I would like to send a special thank to TEM laboratory at VNU University of Science for facilitating me in experiments

Finally, I would like to thank 6G members (Hokkaido University) for discussion and support me during I study. Especially, I would like to thank Shivaji Saha for supporting discussion, reviews.

Contents

List of figures

List of Table

1. Introduction

It has been well known today that the lithosphere (plate), which was originally assumed rigid, is pervasively plastically deformed. Most of the ductile strain occurs in the lithosphere, both in the crust and the mantle (e.g., Vauchez et al., 2012, Fossen et al, 2017). Such fault zones often contain exhumed fault rocks with textures that provide information about the deformation conditions and mechanisms occurring at depth (e.g., Sibson, 1977; Schmid and Handy, 1991). Thus, studying fault rocks that are exposed at the surface may help understand the development of fault zone in ancient time.

In western Mie Prefecture, the Median Tectonic Line (MTL) fault zone which formed at deeper crustal levels in the Late Cretaceous are well preserved, which provides us with a good example for studies on large-scale fault development at depth (Fig. 2.1; 2.2). In this area, several previous studies provide constraints on the tectonic history and deformation condition of the MTL (e.g., Takagi, 1986; Jefferies et al., 2006a, b; Okudaira and Shigematsu, 2012; Shigematsu et al. 2012, 2017; Takagi et al. 2012; Mori et al. 2015). In this study, I analyze the development of the Median Tectonic Line fault zone in SW Japan, based on mesoscopic structural analyses in surface outcrops of the fault and microstructural analyses of fault rocks, particularly focusing on the zone of mylonitic rocks in the northern area from the MTL along the Akaiwadani-River, which originated from the Cretaceous Ryoke granitic rocks (Fig. 3.1). I use quartz microstructure and crystallographic preferred orientation (CPO) and K-feldspar microstructure to infer deformation conditions (i.e. stress, strain rate, and temperature) and analyze the development of fault zone during exhumation based on these deformation conditions. Further, based on the spatial distribution of fault rocks which deformed at different physical conditions, I have investigated how deformation becomes localized in narrow zones along the MTL and plausible mechanisms for strain localization.

2. Geological setting

The Median Tectonic Line (MTL) is a major strike-slip fault system with the largest onshore structural break in southwestern Japan that has been defined as the boundary fault between the Cretaceous Sambagawa high-P/low-T metamorphic belt and Cretaceous Ryoke low-P/high-T metamorphic belt intruded by Cretaceous granitoids, both of which originated from Jurassic to Cretaceous accretionary sediments (Ichikawa, 1980; Ohotomo, 1993; Ito et al., 1996, 2009; Sakashima et al., 2003, Shigematsu et al., 2012, Fig. 2.1a; Fig. 2.2; Fig. 2.3). The MTL extends from eastern Kyushu to Kanto Mts over 1000 km. Displacement estimates along the MTL are uncertain and range between 200 to 1000 km (Ichikawa, 1980; Takasu and Dallmeyer, 1990; Sakashima et al., 2003). The granitoids in the Ryoke belt are variably mylonitized in a zone up to 5 km wide at the north of the MTL (Hara et al., 1980; Takagi, 1986). Although the MTL at the surface dips north at c. 60° in the study area as mentioned below, eastern Kinki, the seismic reflection studies conducted in eastern Shikoku suggest that the fault dips north at around 35° from the surface to about 5 km depth (Ito et al., 1996).

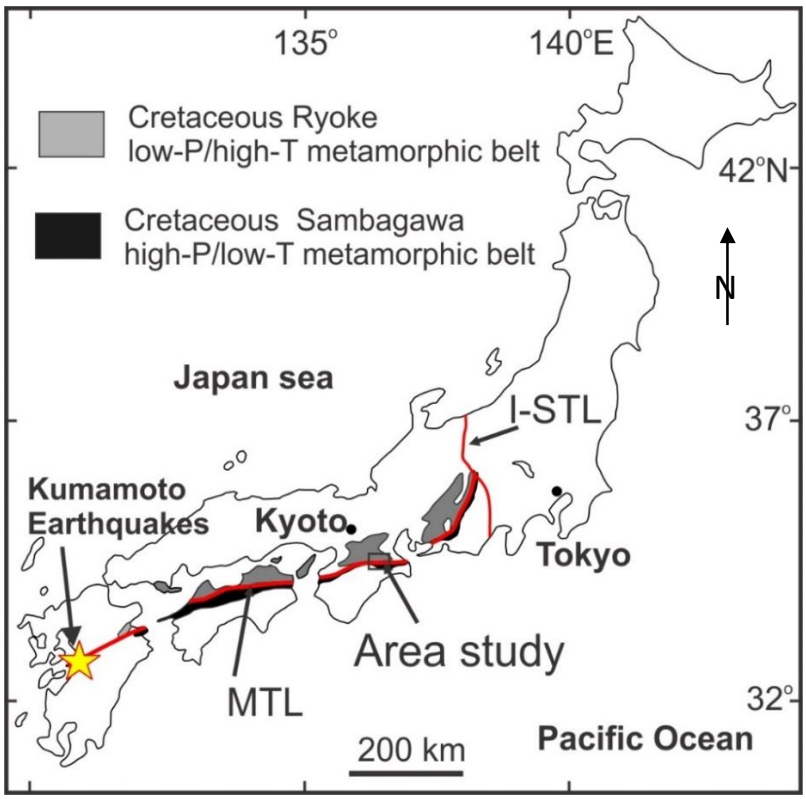

Figure 2.1. Location of the Median Tectonic Line (MTL) in south west Japan marking the boundary between Ryoke metamorphic belt and Sambagawa metamorphic belt. Black box in the map indicate study area in figure 2.2. I-STL: Itoigawa-Shizuoka Tectonic Line

The movement history of the MTL has been divided into several stages when it accommodated deformation under various stress fields and kinematic conditions. The movement of the MTL started in the Late Cretaceous which formed granitic mylonite zones centered in the southern marginal part of the Ryoke Belt (Ichikawa, 1980; Shimada et al., 1998). During the Late Cretaceous, left-lateral strike-slip motion occurred along the proto-MTL (i.e. southern marginal shear zone, e.g. Sakakibara, 1995; Shimada et al., 1998), in relation to oblique subduction at the trench (Ichikawa, 1980; Takagi, 1986; Ito et al., 1996, 2009; Sakashima et al., 2003, Kubota and Takeshita, 2008). At the latest Cretaceous, formation and deposition of the Izumi Group, which unconformably lies on the Cretaceous Ryoke metamorphic rocks and granitoids, occurred as pull-apart basins caused by left-lateral strike-slip motion along the MTL (Miyata, 1990; Noda et al., 2017). In the Palaeocene at c. 60 Ma, the Ryoke metamorphic rocks and granitoids were juxtaposed against the Sambagawa metamorphic rocks, which is caused by large-scale normal faulting along the MTL (Ichinokawa phase, Kubota and Takeshita, 2008). Subsequently, left-lateral strike slip faulting with the component of north-side up occurred along en échelon arranged faults, which were newly formed parallel to and at the north of the MTL in the Middle Eocene at c. 50-40 Ma (pre-Tobe phase, Kubota and Takeshita, 2008, manuscript in preparation). During the earliest Middle Miocene (c. 15 Ma), thrusting occurred in the Shikoku region along the MTL (Tobe phase) which could have been followed by normal faulting (Takagi et al., 1992; Takeshita, 1993; Fukunari and Wallis, 2007; Famin et., 2014). In the Pleistocene at c. 2 Ma, thrusting along the MTL has been reported in the Shikoku and Kinki regions (Shoubudani phase, Huzita, 1980; Okada, 1980). Since a few tens million years ago, the MTL has been reactivated as a major active fault in southwest Japan with right-lateral strike-slip motion (Huzita, 1980; Okada, 2012).

In the area around the Tsukide region, Mie Prefecture, outcrops of the Ryoke granitoids are widely exposed on the northern side of the MTL, while the Sambagawa metamorphic rocks are exposed on the southern side, which is partly covered by alluvial deposits along some rivers (Fig. 2.2b). Based on the correlation between outcrop and borehole data, Shigematsu et al. (2012) inferred that the MTL fault plane strikes N86^{o} E and dip north at 56^{o} in the eastern part c. 10 km apart from the study area, which is also confirmed by observations of outcrops at a few localities in the study area, where the MTL is exposed. The major strand of the MTL fault zone in the Ryoke granitoids is characterized by approximately 70 m thick intensively fractured rocks (cataclasite), where fractured ultramylonites are included, which are surrounded by a damage zone of

a few hundred meters thick formed in protomylonite and little mylonitized rocks (Czertowicz et al., in press), which originated from the Hatai Tonalite (Takagi, 1985; Shigematsu et al, 2012).

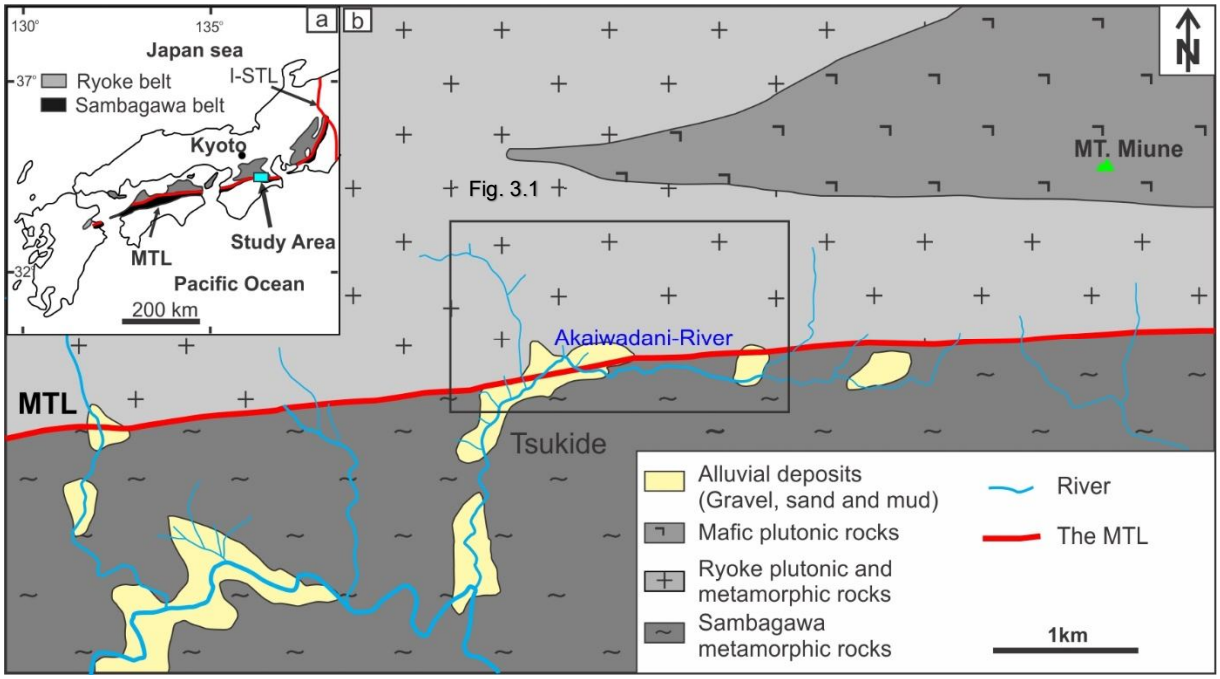

Figure 2.2. Geological map of the Median Tectonic Line fault zone, Mie Prefecture after the Seamless Digital Geological Map of Japan, 1:200000. MTL: Median Tectonic Line; I-STL: Itoigawa-Shizuoka Tectonic Line

However, this study following the original finding by Czertowicz et al. (submitted) will document a very thick mylonite zone more than a few hundred meters located at the position c. 350-800 m north from the MTL, which originated from the Mitsue Granodiorite (Ohira, 1982). The protomylonite, mylonite and ultramylonite in the study area were formed during left-lateral deformation, and then was overprinted by brittle deformation at shallow crustal levels as the shear zone is elevated, resulting in the development of cataclasite, fault breccia and fault gouge (Takagi, 1985; Sakakibara, 1996; Okudaira et al, 2009, Shigematsu et al, 2012, 2017). The protomylonite, mylonite and ultramylonite were formed at various temperature conditions during cooling of the Ryoke granitoids, which is shown by various c-axis fabric patterns of recrystallized quartz grains constituting the mylonites: X-maximum, type II crossed girdles with Y-maximum and type I crossed girdles indicating prism<c> and prism<a>slip, prism<a> and basal<a>, and rhomb<a> and basal<a> slip, respectively (e.g. Sakakibara, 1996).

Figure 2.3. The outcrop of the MTL which separates the Sambagawa metamorphic belt from Ryoke metamorphic belt in the Mie Prefecture.

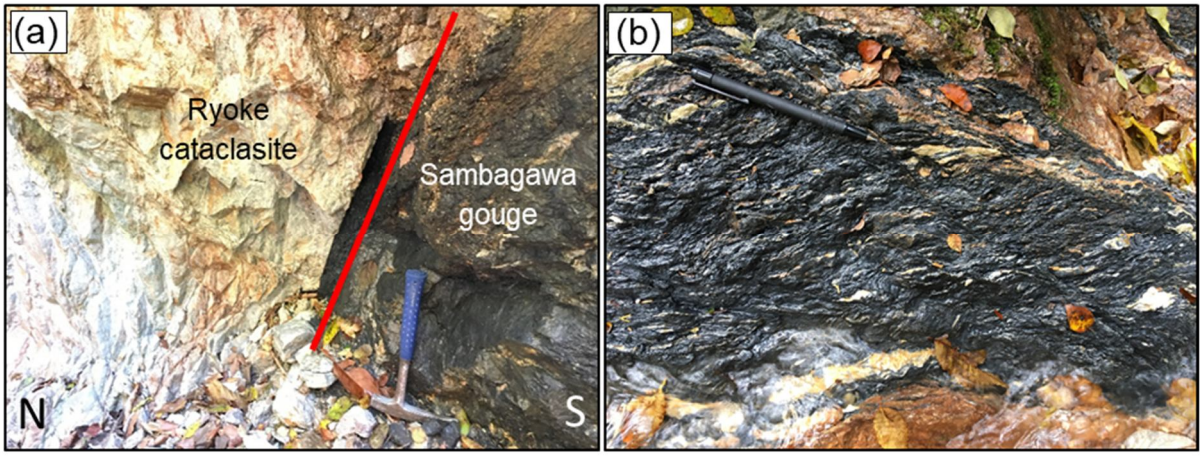

Figure 2.4 Photographs showing the MTL fault rocks in outcrops. (a) The contact between the Ryoke rocks and the Sambagawa schist. (b) Outcrop of Sambagawa schist.

3. Geology of the study area and sample description

In the study area, I mostly focus on the zone of mylonitic rocks in the northern area from the MTL, which is up to c. 800 m wide along the Akaiwadani-River (Fig. 3.1). This area is mapped as the Mitsue granodiorite (Ohira, 1982), which is characterized by K-feldspar megacryst. However, the detailed mapping revealed that the area up to c. 300 m wide from the MTL (Area A) mostly consists of protomylonite, which originated from tonalite (Fig. 3.1, Fig. 3.2a, Fig. 3.3a), and the area further north (Area B) consists of mylonite, which originated from granite (Fig. 3.1, Fig. 3.2b, Fig. 3.3b; Fig. 3.4), correlated with the Mitsue granodiorite (Ohira, 1982). I systematically measured the orientations of foliations. The foliation strikes E-W and dips north at a high angle. Seventeen orientated samples (Table 3.1) are collected along the Akaiwadani-River and adjacent rivers, the localities of which are in shown in (Fig. 3.1). 7 tonalitic protomylonite samples were exclusively collected in Area A along the MTL, while 10 granitic mylonite samples were exclusively collected from Area B which is more 300-800 m apart from the MTL (Table 3.1).

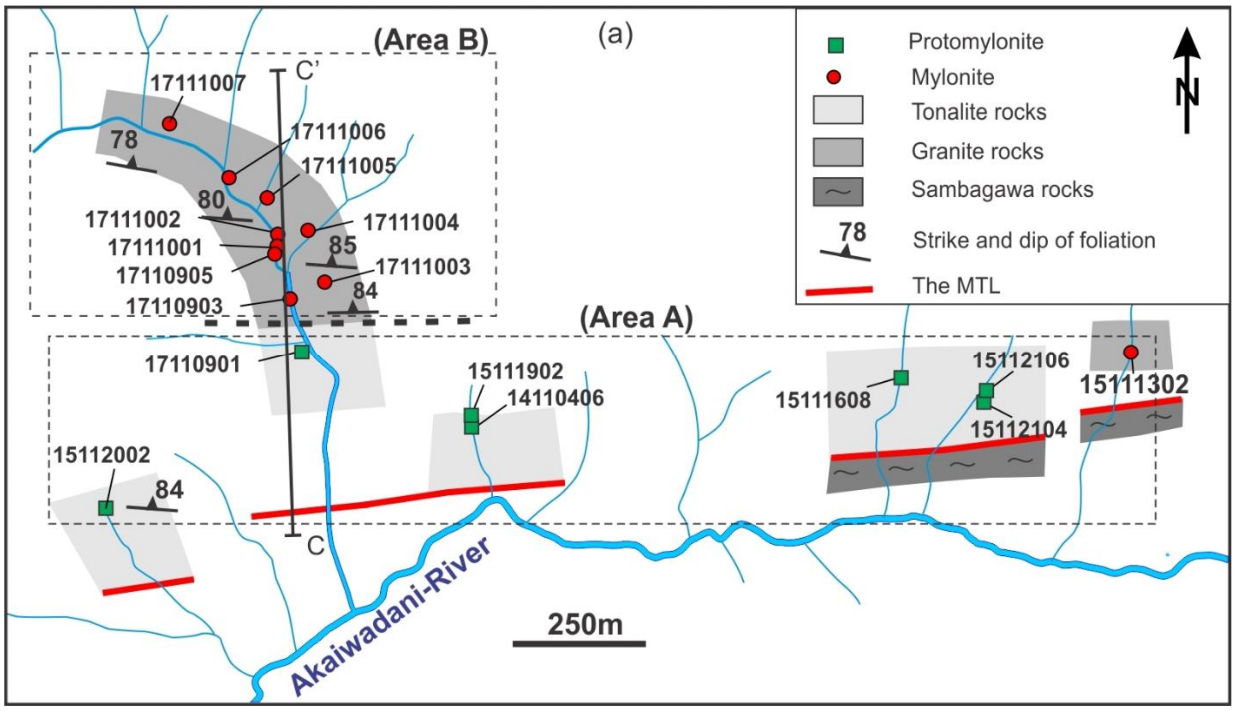

Figure 3.1. The sample locations map at the MTL, showing lithology and attitude of the mylonitic foliation. Area A mostly consists of protomylonite while Area B comprises of mylonite.

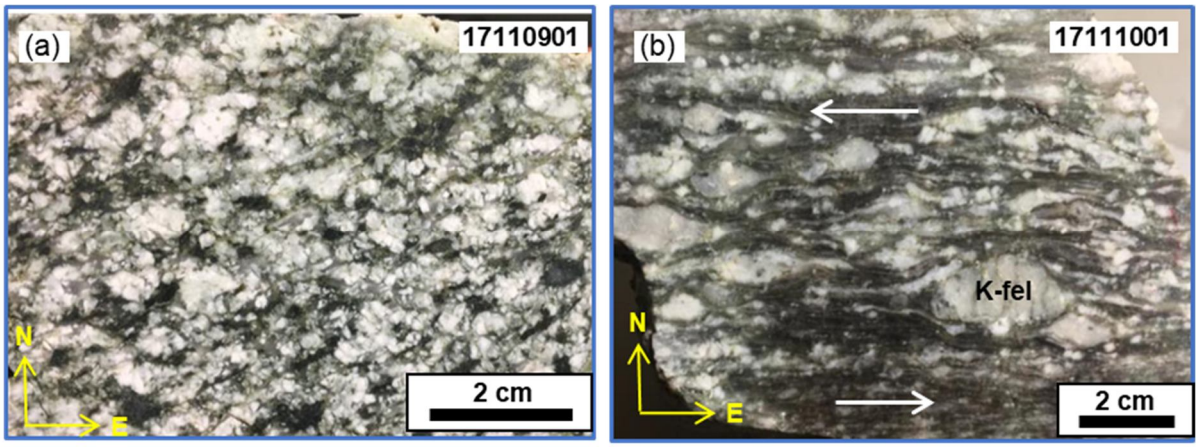

Figure 3.2 Polished hand specimens in proto-mylonite and mylonite from the MTL. (a) Less deformed protomylonite sample from Area A. (b) Asymmetric trails of stretched plagioclase around porphyroclast of K-feldspar from mylonite of Area B indicating sinistral shear sense (top to the west).

In Area A, protomylonite samples consist of plagioclase, quartz, chloritized mafic minerals, muscovite altered from plagioclase, and calcite veins (Fig. 3.2a; Fig. 3.3a). Some protomylonite samples consist of quartz ribbon surrounding relict quartz grains (Fig. 5.2a, b). The percentage of quartz, alkali feldspar and plagioclase in the samples were calculated by the point counting method using optical microscopic with more than 500 points analyses for each thin section showing the absence or rareness of alkali feldspar (Table 3.1). Plotting the results on the QAP diagram that used to classify igneous rocks with visible mineral grains from their feldspar and quartz content (after Streckeisen, 1976) indicated the protomylonite samples from Area A originated from tonalite (Fig. 3.5).

In Area B, mylonite samples consist of k-feldspar porphyroclast, plagioclase, quartz ribbon, biotite, muscovite altered from plagioclase, and calcite veins (Fig. 3.2b; Fig. 3.3b; Fig. 3.4). The asymmetric K-feldspar porphyroclasts (σ texture) indicating sinistral shear (north to the west) (Fig. 3.2) that characterize the motion at the Kashio phase during the Late Cretaceous (Ichikawa, 1980; Takagi, 1986; Sakakibara, 1995; Shimada et al., 1998; Kubota and Takeshita, 2008). The S/C' texture that commonly developed in mylonites (Lister and Snoke, 1984) also indicates sinistral shear (Fig. 3.4a). The result of calculating the percentage of quartz, alkali feldspar and plagioclase in the samples by the point counting method was presented in Table 3.1 and the QAP diagram, indicating that the mylonite samples from Area B originated from granite (Fig. 3.5).

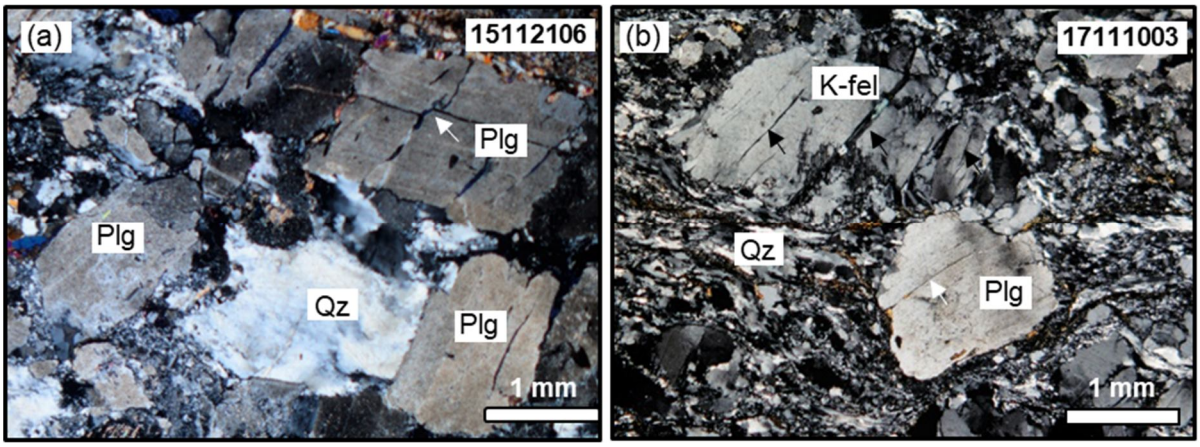

Figure 3.3 Crossed polarized light microphotographs of the mylonitic samples. (a) Tonalitic rock consists of plagioclase, quartz from Area A. (b) Granitic rock consists of K-feldspar, plagioclase porphyroclast and deformed quartz from Area B.

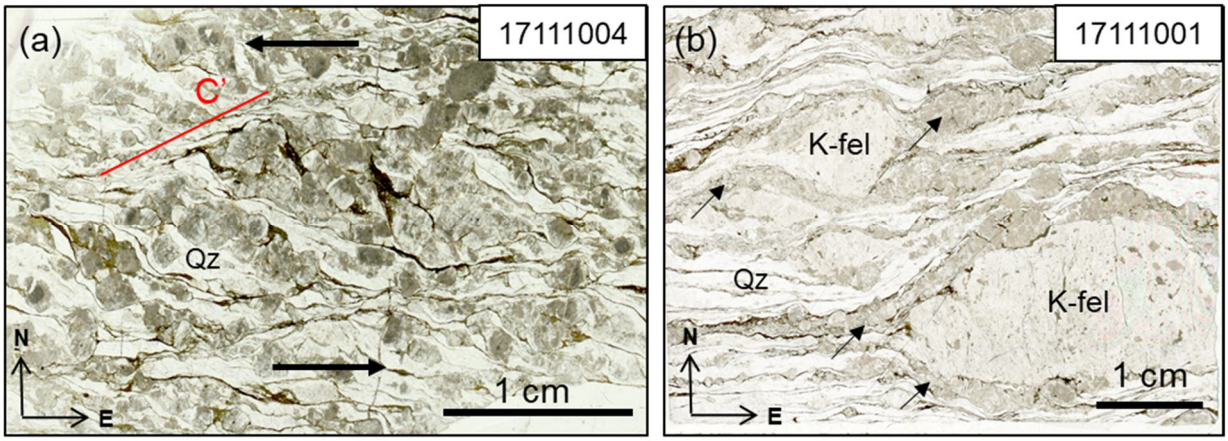

Figure 3.4. Plane polarized light photograph of whole thin section of the mylonite samples from Area B. (a) S/C' fabric indicating sinistral shear sense (top to the west). (b) Large K-feldspar porphyroclasts are surrounded by plagioclase layers (black arrows) and quartz.

Table 3.1. Summary of modal percentage of constituent minerals from the protomylonite and mylonite samples

Sample No.	Northward distance from MTL (m)	Lithology	Modal percentage		
			%Q	%K-fel	%Plg
Area A					
14110406	103	Tonalitic proto-mylonite	37.07	0.33	62.60
15112002	105	Tonalitic proto-mylonite	38.52	1.77	59.71
15111902	119	Tonalitic proto-mylonite	25.32	0.00	74.68
15111608	126	Tonalitic proto-mylonite	42.23	0.16	57.61
15112104	132	Tonalitic proto-mylonite	35.96	0.00	64.04
15112106	158	Tonalitic proto-mylonite	40.75	0.00	59.25
15111302	184	Granitic mylonite	42.03	22.63	35.34
17110901	248	Tonalitic proto-mylonite	33.10	2.25	64.64
Area B					
17110903	339	Granitic mylonite	32.57	26.87	40.55
17111003	379	Granitic mylonite	34.28	33.38	32.34
17110905	421	Granitic mylonite	34.67	25.00	40.33
17111001	429	Granitic mylonite	34.83	36.63	28.54
17111002	462	Granitic mylonite	34.69	29.71	35.60
17111004	490	Granitic mylonite	28.01	40.92	31.07
17111005	520	Granitic mylonite	45.16	31.80	23.04
17111006	585	Granitic mylonite	34.13	50.52	15.35
17111007	711	Granitic mylonite	41.69	40.94	17.37

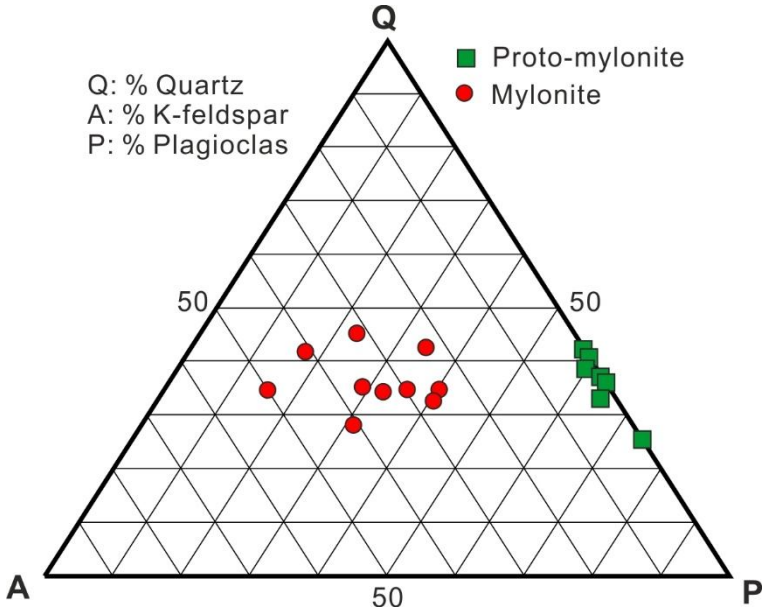

Figure 3.5. Classification of proto-mylonite and mylonoite based on mineralogic composition by using the QAP diagram of Streckeisen (1976).

4. Methods

Three types of microstructural analyses with electron-backscattered diffraction (EBSD), transmission electron microscope (TEM) and electron-probe microanalyzer (EPMA) have been conducted to elucidate crystallographic preferred orientation (CPO), dislocation substructures of recrystallized quartz in mylonites, and microchemistry of two-feldspars (K-feldspar and plagioclase) in mylonite, respectively.

4.1. EBSD analysis

For EBSD analysis, all 17 samples were prepared as polished thin sections. For each sample, one thin section was made, which is cut normal to the foliation and parallel to the lineation (i.e. XZ section), Three protomylonite samples, where the orientation of lineation is uncertain, were cut parallel to foliation (i.e. XY section). Here, the X-, Z- and Y-axes are elongation, shortening and the intermediate axes of finite strain, respectively. Then, they were polished using diamond paste, followed by colloidal silica polishing. EBSD analysis was conducted on carbon-coated samples in a JEOL JIB-4600F/HKD field-emission gun scanning electron microscope (FEG–SEM) at a voltage of 15 kV and a working distance of ~25 mm at Hokkaido University, Japan. EBSD patterns were measured by an Oxford Instruments detector and indexed and processed using the Oxford Instruments Aztec software package.

Because of the heterogeneous deformation and recrystallization in the samples, I conducted the point analysis to analyze the c-axis crystallographic orientation of quartz. For each sample, 500 to 1000 points were randomly selected for quartz aggregates in the thin section. To quantify the strength and shape of quartz c-axis fabric I calculated the eigenvalues of the orientation tensor (Woodcock, 1977) determined with the Stereonet program by Allemendinger (1988). Fabric strength was quantified using the "intensity" parameter of Lisle (1985), defined as:

$$FI = \frac{15}{2}\sum_{i=1}^{3}\left(\lambda_i - \frac{1}{3}\right)^2 \tag{4.1}$$

where FI = intensity and λi = eigenvalues. PGR ternary diagram is calculated from the acquired eigenvalues, which measures the degree to which the orientation data tends to be a Point (P), girdle (G) and random (R) distribution (Vollmer, 1990) Here, P = λ1 – λ2, G = 2(λ2 – λ3), R = 3λ3, where λ1–3 represent the eigenvalues of the normalized orientation tensor.

The shape preferred orientation (SPO) and grains size of quartz were analyzed

by the mapping analysis with the same EBSD analysis condition. Step size was chosen to analyze smaller than one-fifth of the diameter of the smallest recrystallized grains for each sample (Cross et al., 2017). To reduce the noise in the EBSD data, I have used the HKL Channel 5 software package. Pixels with no solution were reduced using a five-neighbor extrapolation, and "wild spikes" were removed. Using misorientation angle higher 10° to define the grain boundaries of quartz, I obtained quartz microstructures in terms of aspect ratio (R, grain length/grain width) and shape factor (Takeshita and El-Fakharani 2013). The aspect ratio of each recrystallized grain is calculated as follows.

$$R = a/b \tag{4.2}$$

where R is aspect ratio, a is grain length and b is grain width.

Intracrystalline lattice distortion is proportional to dislocation density which gives the misorientation angle between every pixel in a grain and the mean orientation of that grain that are analyzed by EBSD data. So, the recrystallized grains can be separated from relict grains by quantifying the degree of intracrystalline lattice distortion in each grain. In this study, I used the grain orientation spread (GOS) that followed the method presented by Cross et al. (2017) for separating recrystallized and relict grains of quartz (Fig. 4.1). The GOS of each grain which is equivalent to the average mis2mean value of each grain (Wright et al., 2011).

$$\mathrm{GOS} = \frac{1}{\mathrm{N}}\sum_{i=1}^{\mathrm{N}} M_i \tag{4.3}$$

where GOS- the grain orientation spread (o), N- a number of pixels, Mi- the misorientation between each pixel in a grain and the mean orientation of that grain (o).

Plotting the GOS threshold versus differential stress for all samples reveals a positive correlation, reflecting an overall increase in lattice distortion with stress, corresponding to an increase in dislocation density (Table 5.1). The average recrystallized grain size was calculated as the root mean square (RMS) of the recrystallized grains (Table 5. 1).

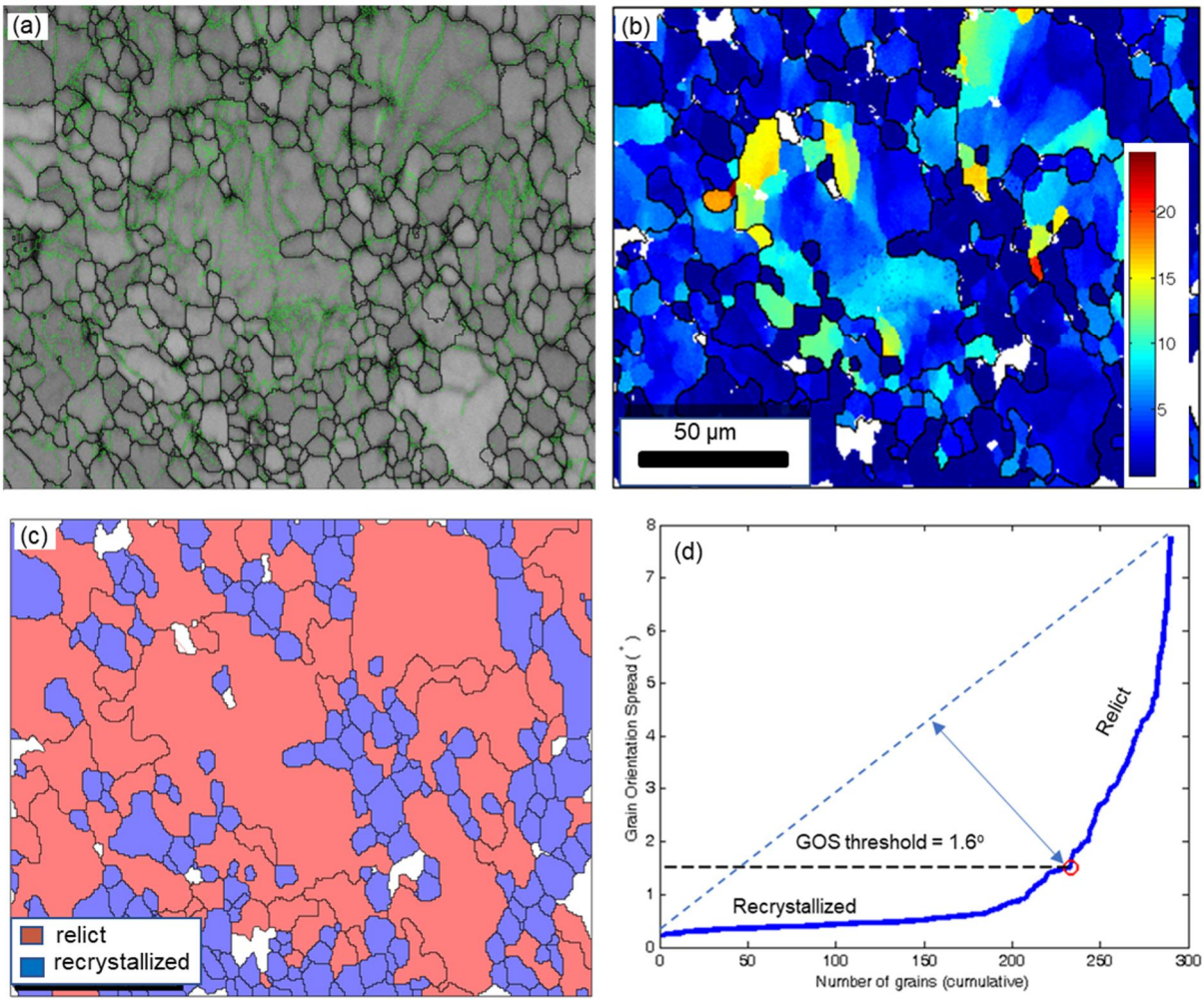

Figure 4.1 Example for the separation the recrystallized grains and relict grains from the EBSD map data following the method presented by Cross et al. (2017). (a) Band contract map of from EBSD data showing boundaries of grain and subgrain: black line and green line, respectively. (b) Map of the misorientation between each pixel in a grain and the mean orientation of that grain (mis2mean). (c) GOS based isolation of recrystallized and relict grains. (d) a cumulative plot of the number of grains versus the grain orientation spread (GOS). The knee in the curve gives the threshold between recrystallized and relict grains.

4.2. TEM analysis

The transmission electron microscope (TEM) allows the analysis of submicroscopic quartz structure, with a resolution below one micron. Observation of dislocations by a TEM has been conducted to determine the slip systems operative in deformed quartz (Lister et al., 1978; Takeshita and Wenk, 1988). The arrangement and densities of dislocation and the subgrain structure quartz aggregate were analyzed with

the FEI Tecnai G2-20 Twin TEM installed at VNU University of Science and the JEOL JEM-2010 installed at Hiroshima University. For TEM analyses, the selected areas in thin sections were thinned by ion milling in a Gatan Precision Ion Polishing System Model 691 until electron transparency was reached (± 0.1 µm thick). The TEM foils samples were carbon coated at 5 µm thickness. The TEM images were acquired at an acceleration voltage of 200 kV and an electric current of 120 nA. I employed a conventional bright field (BF) imaging technique (McLaren & Hobbs, 1972; McLaren, 1991). Areas which diffract strongly cause an intensity loss of the transmitted beam and appear dark. A fully intact crystal is transparent, whereas crystal defects strongly diffract the electron beam. Thus dislocations, twins, subgrain- and grain-boundaries are observed as dark lines.

The dislocation density (ρ=L/V [cm^3/cm], where V is the selected volume of crystal containing dislocations, and L is the total length of dislocations) was calculated from TEM images by following the simple formula (e.g. Ando et al, 1993).

$$\rho = N/S \ [1/cm^2] \qquad (4.4)$$

where N and S are the number of free dislocations (*Fig. 4.2*) and the measured area, respectively. 30 to 50 areas with the size 3 µm x 5 µm for each type of mylonite are used to calculate dislocation density.

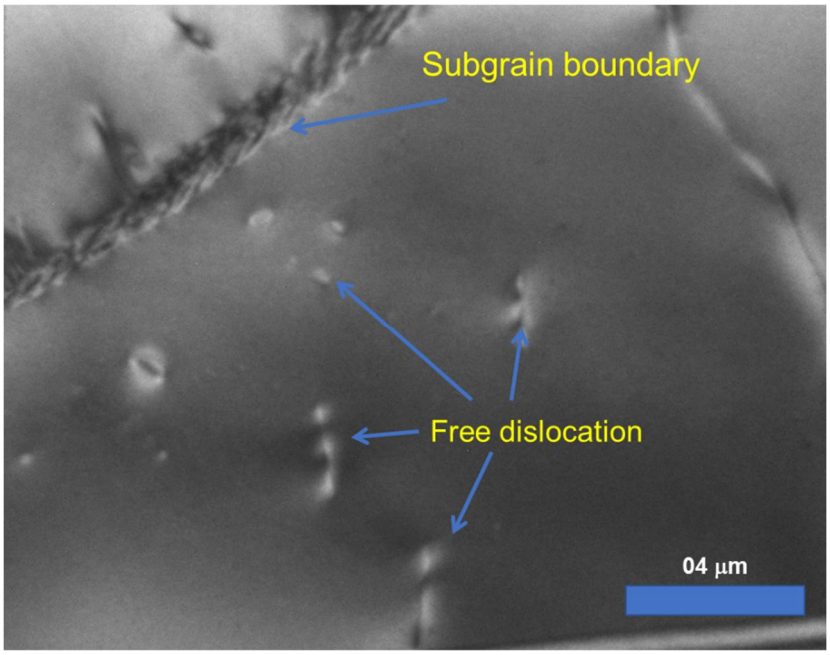

Figure 4.2 TEM micrograph showing free dislocation and subgrain boundary

The relationship between the free dislocation density in quartz and the flow stress is given by the relation.

$$\sigma = C \times \rho^{p} \qquad (4.5)$$

where σ is the steady-state differential stress in MPa; ρ is the dislocation density in cm^{-2}. $C = 1.64 \times 10^{-4}$, and $p = 0.66$ (McCormick, 1977; Ord and Christie, 1984).

4.3. EPMA analysis

For EPMA analysis, I selected 9 granitic mylonite samples from the area study. The composition of two feldspars was carried out using an Electron probe micro-analyzer (EPMA) JEOL JXA-8800R installed at Hokkaido University, Japan. The analytical conditions were 15 kV accelerating voltage, 20 nA probe current and 2 µm probe diameter. The thin sections also were carbon coated. The Two feldspar thermometer was used to determine the deformation temperature in mylonite rocks, which can be inferred from the composition of two feldspars in myrmekite texture (Table 5.3; Stormer, 1975; Stormer & Whitney, 1977). The feldspar compositions were calculated from atomic numbers of Na, K, and Ca assuming Si, Al and O were in stoichiometric proportions. Each sample analysis represents the average of 3 to 5 spots on a single grain (Fig. 4.3).

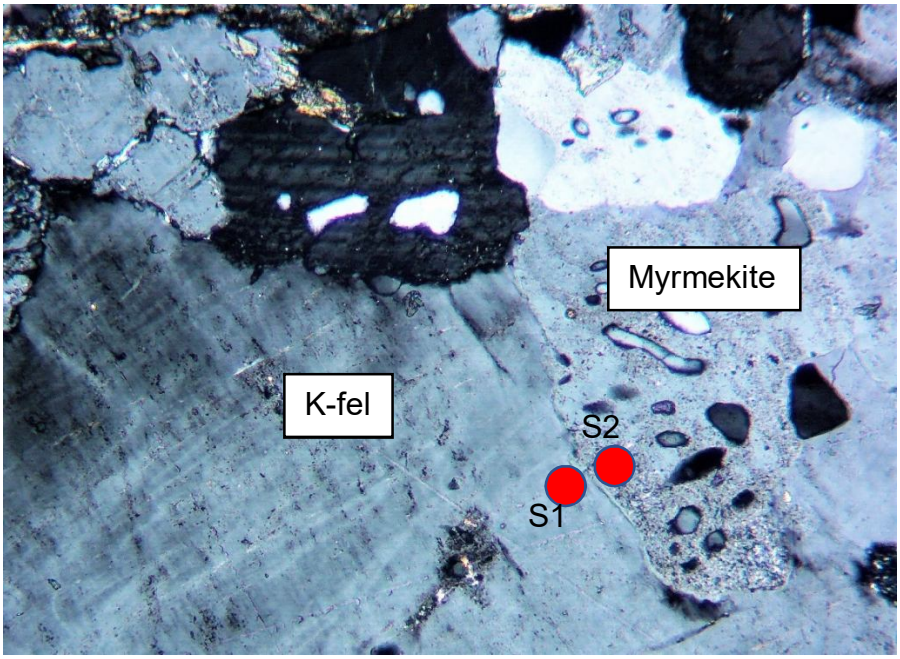

Figure 4.3: Analysis composition for two feldspar thermometers, S1 and S2 are spots measured in K-feldspar and plagioclases, respectively.

5. Results

5.1. Microstructure of quartz

As mentioned in the previous section, the study area can be divided into the two areas: Area A in proximity to the MTL, which mostly consists of protomylonite originated from tonalite and up to c. 300 m wide (Fig. 3.1; Fig. 5.1), and the area further north (Area B), which consists of mylonite originated from granite (Fig. 3.1; Fig. 5.1). Detailed optical microscopic (OM) observations and the EBSD, however, revealed that the quartz microstructures are highly variable. In prticular, in Area B, mylonites are divided into two types with S-type and P-type quartz microstructures (Masuda and Fujimura, 1981) (Fig. 5.1). In this section, microstructures of quartz will be described separately for the areas A and B.

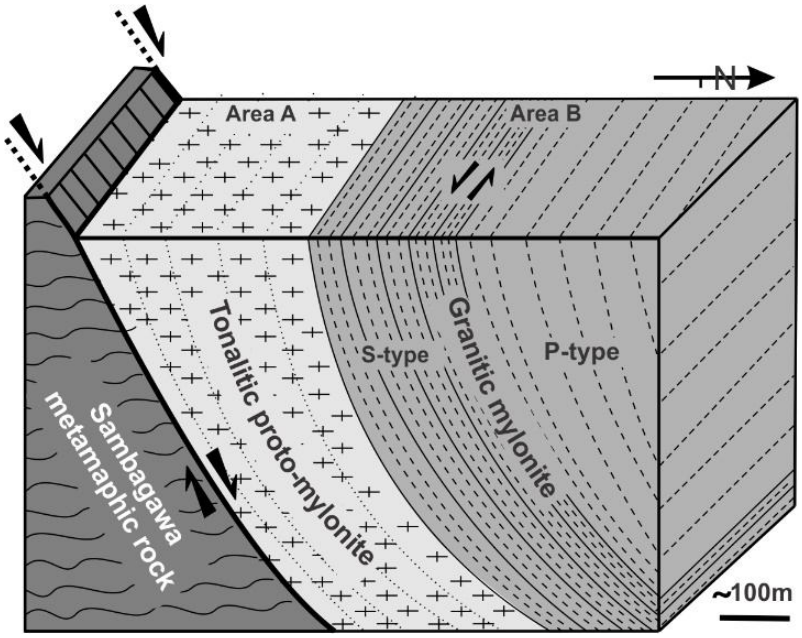

Figure 5.1. Cross-section across the line CC' in Fig. 3.1 showing distribution of the MTL fault rocks.

5.1.1 Optical microscopic (OM) observation

Quartz microstructures in the area A greatly varied. In the protomylonite, some of the quartz grains occur as large (< 3 mm long) (Fig. 3.3a), highly flattened relict grains, showing patchy and undulose extinction, and deformation lamellae (Fig. 5.2a), which are surrounded by equigranular aggregates of recrystallized small grains that are formed by the process of subgrain rotation recrystallisation (SGR) (Guillope and Poirier, 1979; White, 1976; Hirth and Tullis, 1992; Stipp et al, 2002). In some domain recrystallization is mostly completed (Fig. 5.2b).

In some samples (e.g. sample 15112002; 15112004; Fig. 5.2c; Fig. 5.2d), core and mantle structure (Guillope and Poirier, 1979; White, 1976) is developed in ribbon-like highly strained porphyroclasts of quartz by progressive subgrain rotation (SGR). The recrystallized quartz grains formed by SGR completely consumed relict ribbon grains.

In some other samples (e.g. sample 14110406, 1511902; Fig. 5.2e; Fig. 5.2f), grain boundaries bulge into the crystal with high dislocation density and form new small crystals by bulging (BLG) recrystallization (Shigemastsu, 1999; Shigematsu & Tanaka, 2000; Stipp et al., 2002). These microstructures are like those of regimes 1 to 2 described by Hirth and Tullis (1992) in experimentally deformed quartzites.

Area B consists of two types of microstructure across the MTL: S-type mylonite and P-type mylonite (Masuda and Fujimura, 1981) based solely on the microstructure of quartz (Fig. 5.1). The S-type mylonite, which occurred at the positions of 300 m to 490 m northward distance from the MTL, consists of coarse strongly flattened ribbon quartz grains with undulose extinction (Fig. 5.3a) which are surrounded by fine equant quartz recrystallized grains (core-mantle structures, Fig. 5.3 b, d) (Guillope and Poirier, 1979; White, 1976). The microstructure features indicate that the SGR dynamic recrystallization occurred in the S-type mylonite. In several samples, quartz aggerate show oblique foliation structure with angle around 30^{o} (Fig. 5.3c) indicating a top to the left sense of shear (Passchier & Trouw, 1998) which is related to the movement in the Kashio phase during the Late Cretaceous (Ichikawa, 1980; Takagi, 1986; Kubota and Takeshita, 2008).

The P-type mylonite occurred at the positions of 490 m to 800 m northward distance from the MTL (Fig. 5), where recrystallized quartz grains show a smaller aspect ratio, less strongly developed undulatory extinction and lobate grain boundaries with large amplitude sutures (Fig. 5.3e; Fig. 5.3f) which were created by the grain boundary migration (GBM) recrystallization (Poirier and Guillope, 1979).

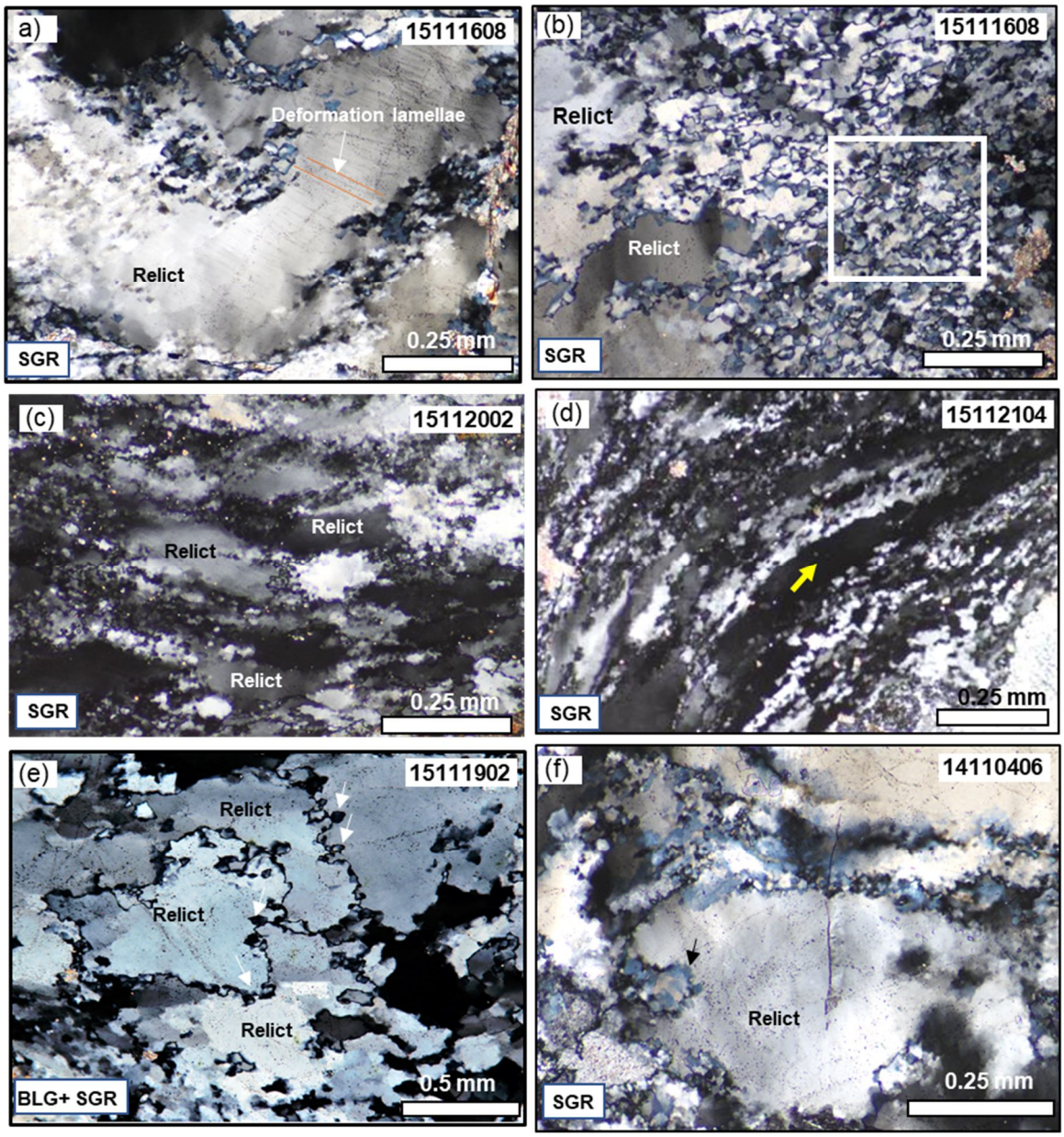

Figure. 5.2 Photomicrographs (crossed polarized light) of microstructural evidences revealed by quartz grains in protomylonite samples from Area A. (a, c, f) relict grain with undulose extinction and deformation lamellae are surrounded by recrystallized small grains because of the SGR. (b) highly recrystallized domain (in box square). (d) Core and mantle structure developed in ribbon-like highly strained porphyroclasts (arrow) by the SGR. (e) grain boundaries bulging (white arrows) because of the BLG recrystallization.

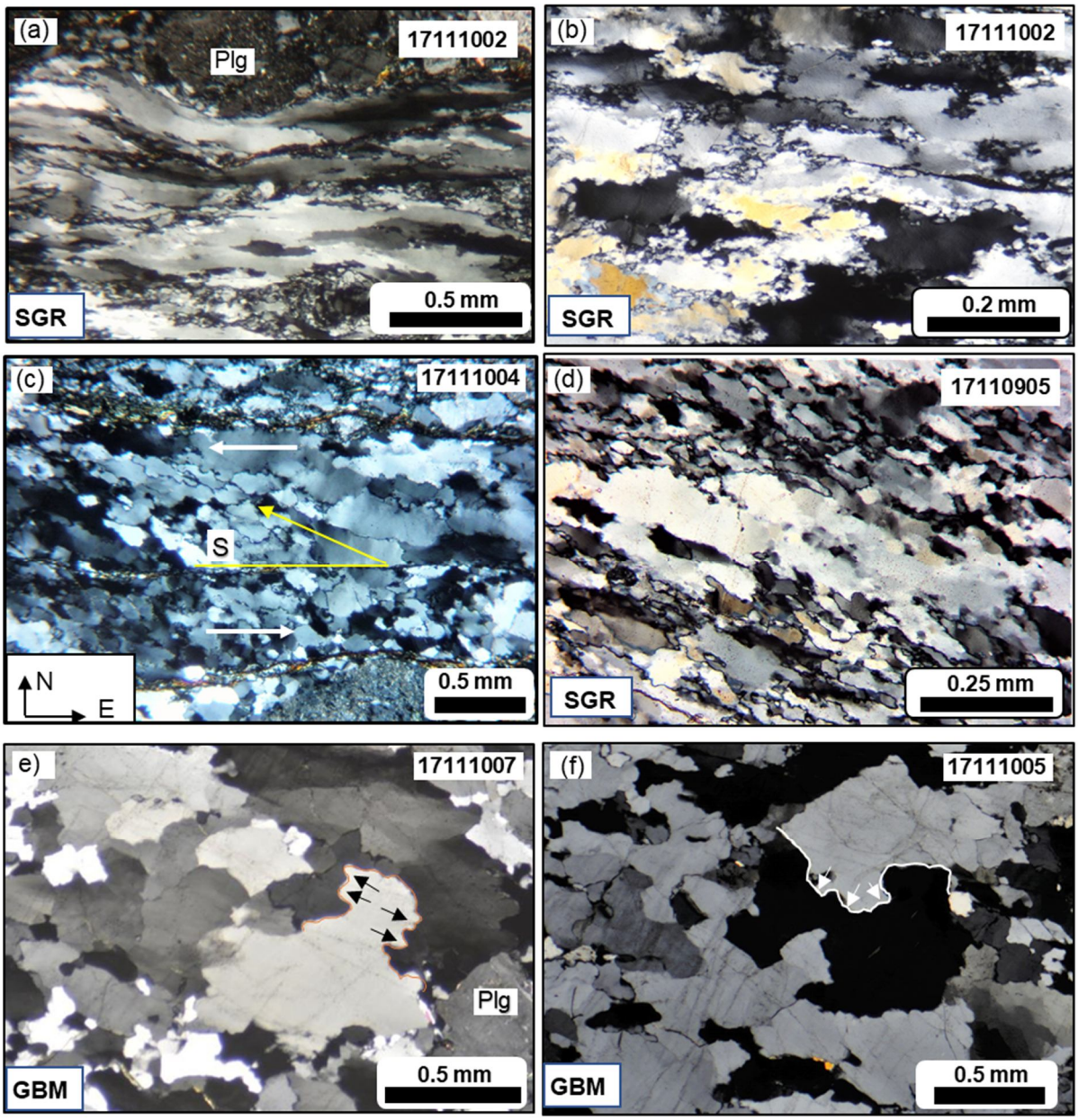

Figure 5.3 Photomicrographs (crossed polarized light) of microstructural evidences revealed by quartz grains in mylonite samples from Area B. (a) S-type mylonite microstructure showing strongly flattened ribbon quartz grains. (b) Core and mantle structure of quartz grains that formed by the SGR in S-type mylonite. (c) oblique foliation structure made up quartz aggerate by making an angle of 30^{o} with the main foliation which indicate a top to the west shear sense in S-type mylonite. (d) Core and mantle structure with higher degree of recrystallization in S-type mylonite. (e, f) P-type mylonite representing the GBM evidenced by the lobate grain boundaries (arrows) with sutures of large amplitude.

5.1.2 Shape preferred orientation (SPO)

The shape factors (see Takeshita and El-Fakharani 2013) as lengths of long (a) and short (b) axes of a best-fit ellipse and the orientation of long axis (i.e. angle ϕ) relative to the reference orientation are calculated for each grain using the HKL Channel 5 software package base on the EBSD data analysis. The R/ϕ diagram (e.g. Ghosh, 1993) are constructed for all the domains from different samples (Fig. 5.4; Fig. 5.5).

In Area A, the aspect ratio (R) of the recrystallized quartz grains are less than 6, and the preferred orientation of the long axis is weak (Fig 5.4). Especially, quartz aggregates in some domain with recrystallized quartz grains related to the BLG recrystallization (Fig. 5.2e) show a very weak preferred orientation of the long axis and small Rs are observed for these samples (e.g. Samples 14110406; 15112106; Fig. 5.4). Further, quartz aggregates in several domains that developed in ribbon-like highly strained porphyroclasts of quartz, the Rs of the recrystallized grains are also low, but show higher preferred orientation (sample 15112002; 15112004; Fig. 5.4) indicating that the development of foliation and lineation are stronger there.

In Area B, the S-type mylonite consists of coarse strongly flattened ribbon quartz grains (Fig. 5.3a) showing a high aspect ratio (R~11) and very high concentrated orientation distribution (e.g. Samples 171101001; 171101002; Fig. 5.5). While the P-type mylonite consists of large recrystallized quartz grains showing lobate grain boundaries with large amplitude sutures and a small aspect ratio and weaker concentration of orientation distribution (e.g. Samples 171101005; 171101006, 171101007; Fig. 5.5). Note sample 171101004 (Fig. 5.5; Fig. 5.3c) that showed the aspect ratio is a transition between high R of S-type mylonite and small R of P-type mylonite suggesting that a transition between S-type mylonite zone and P-type mylonite zone maybe occur around the sample 171101006 location at 490 m northward distance from the MTL.

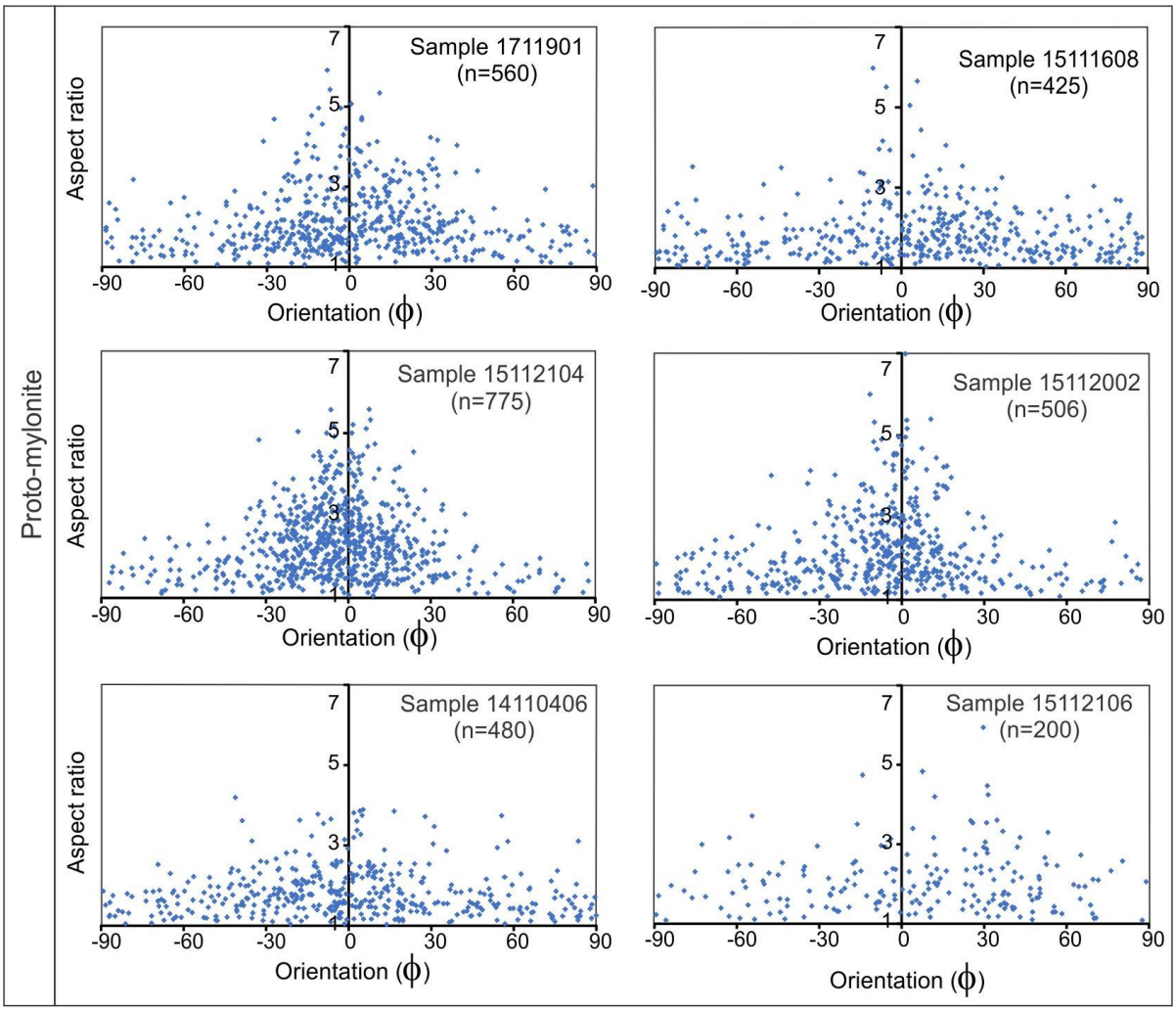

Figure 5.4: Aspect ratio (R) plotted against the orientation of long axis with respect to the foliation (ϕ) for the recrystallized quartz grains in proto-mylonite of the Area A. n = number of analyzed grains.

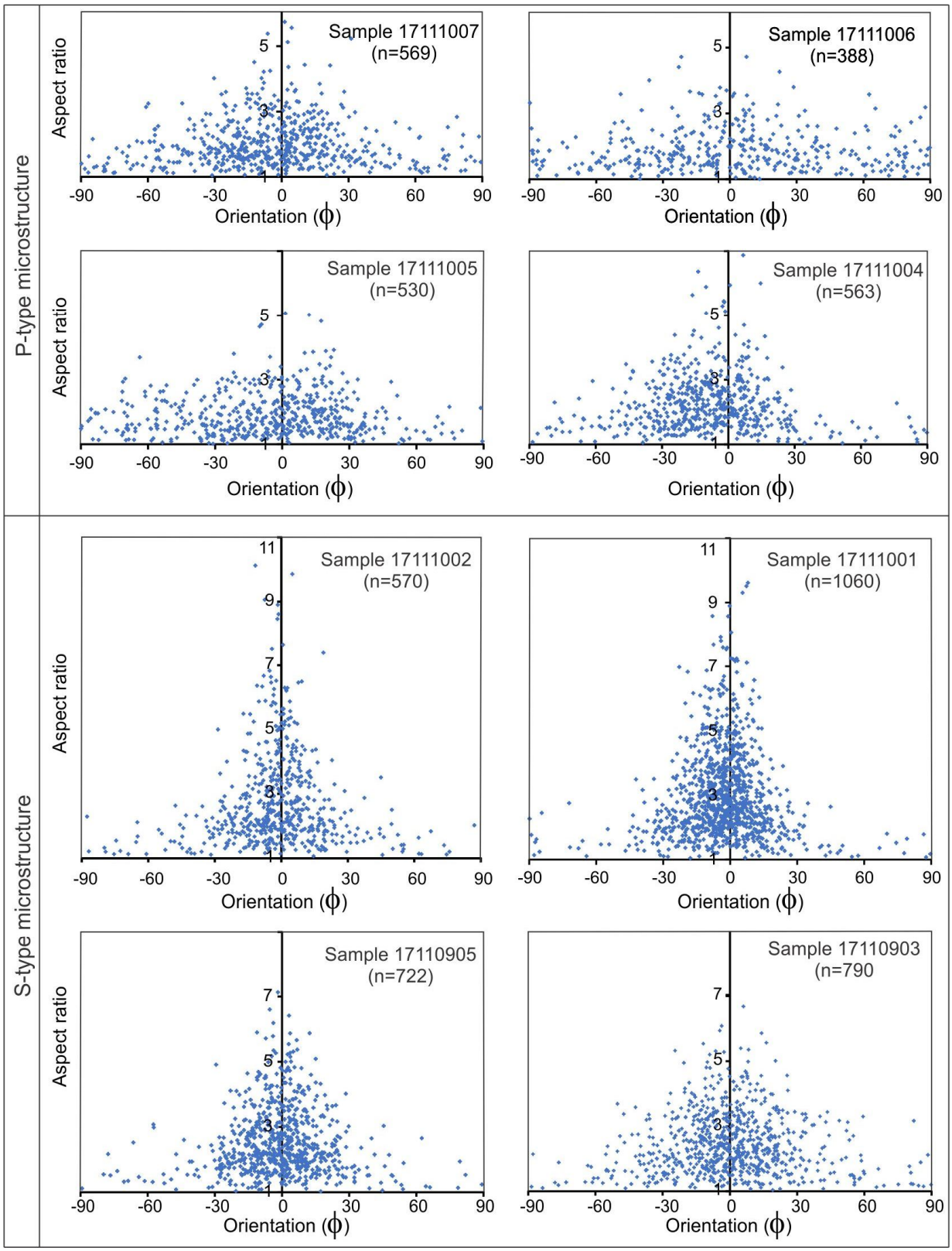

Figure 5.5: Aspect ratio (R) plotted against the orientation of long axis with respect to the foliation (ϕ) for the recrystallized quartz grains in mylonite of the Area B. n = number of analyzed grains.

5.1.3 Recrystallized grain size

The recrystallized grain size of quartz is one of the typical features of the mylonite (e.g. Tullis et al. 1982; Vernon et al, 1983; Takagi, 1986). Grain defined as recrystallized grains are all small while relict grain is mostly large. Some of the recrystallized grains, however, may be small relict grains when they formed early in the deformation history and subsequently accumulated strain. As a result, a population of the relict grain the recrystallized grain is overlapped.

The GOS method that presented by Cross et al. (2017) is based on quantifiably different magnitudes of internal distortion (dislocation density) is effective for deconvolving two overlapping grain size distributions that the two-grain populations have. Data that are analyzed from the EBSD (Fig. 5.6a; Fig 5.7a; Fig. 5.9a; Fig. 5.10a) was used to separate relict and recrystallized grains by MATLAB software using the MTEX "mis2mean" property. The GOS threshold value, GOS-separated recrystallized and relict quartz grains map (Fig 5.6b; Fig 5.7b; Fig. 5.9b; Fig. 5.10b), distribution of $\log_{10}$ grain size (Fig 5.8; Fig 5.11), RMS recrystallized quartz were summarized in table 5.1.

The sizes of recrystallized and relict grains of quartz for promylonite samples in Area A are shown in Figure 5.8, which are determined based on the GOS threshold values (Cross et al., 2017). The diagrams show some peaks of grains size around 70 μm, 30 to 40 μm and less than 10 μm. The mean recrystallized grains size (RMS) of quartz for protomylonite samples in the Area A are a range of 6 μm to 15 μm (Table 1; Fig 5.8). The variation of the mean recrystallized grains size in the samples is generally correlated with distance from the MTL: closer to the MTL the mean recrystallized is smaller (Table 1; Fig. 5.12a). Whereas, the GOS threshold values increases from 2.5^{o} to 4^{o} toward the boundary between the Area A and B (Table 1; Fig 5.12c).

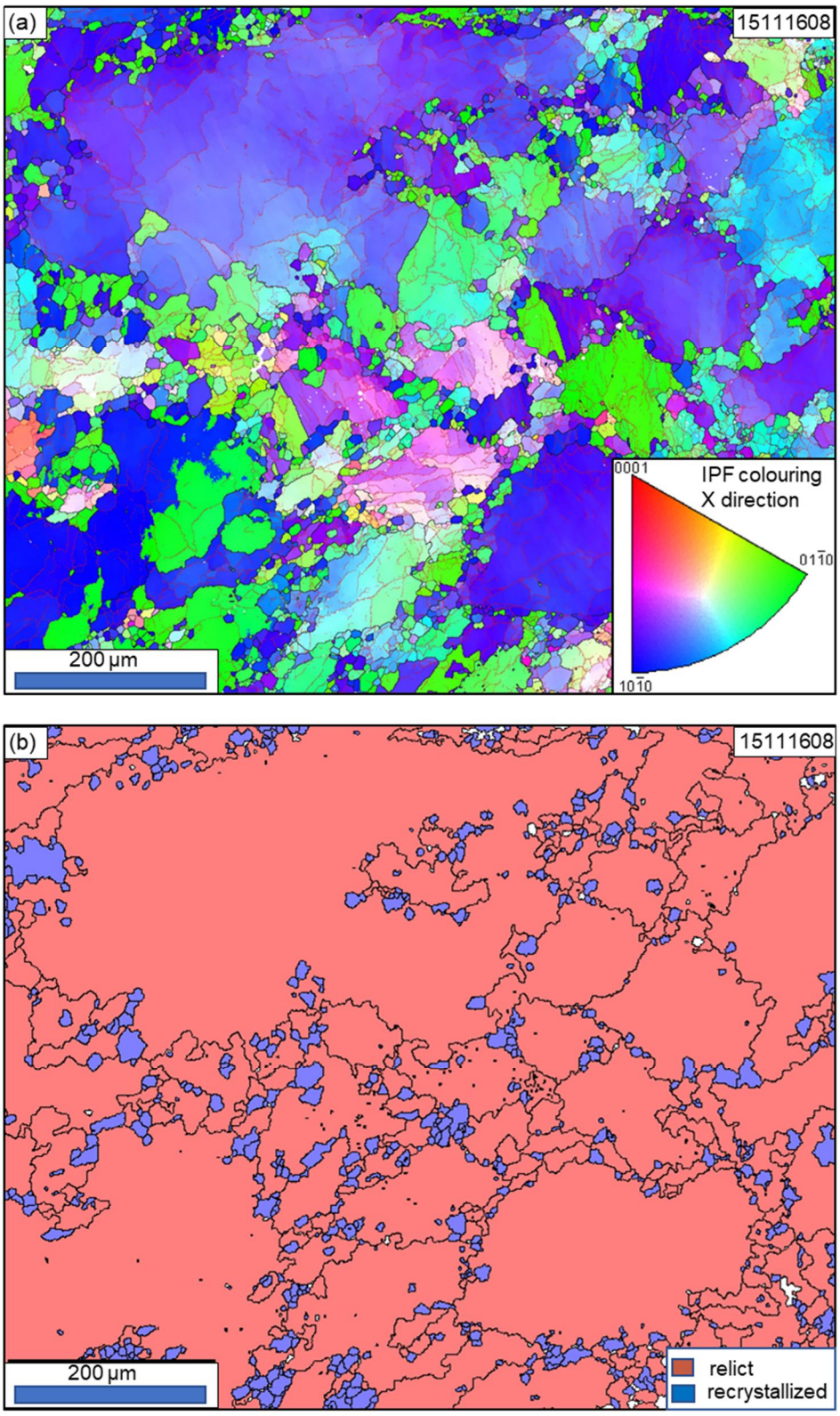

Figure 5.6. EBSD data of sample 15111608 from proto-mylonite of Area A. (a) Quartz inverse pole figure (IPF) map that was constructed by EBSD analysis. Red lines are subgrain boundaries, black lines are grain boundaries. (b) GOS-separated recrystallized and relict quartz grains map from EBSD data following Cross et al. (2017).

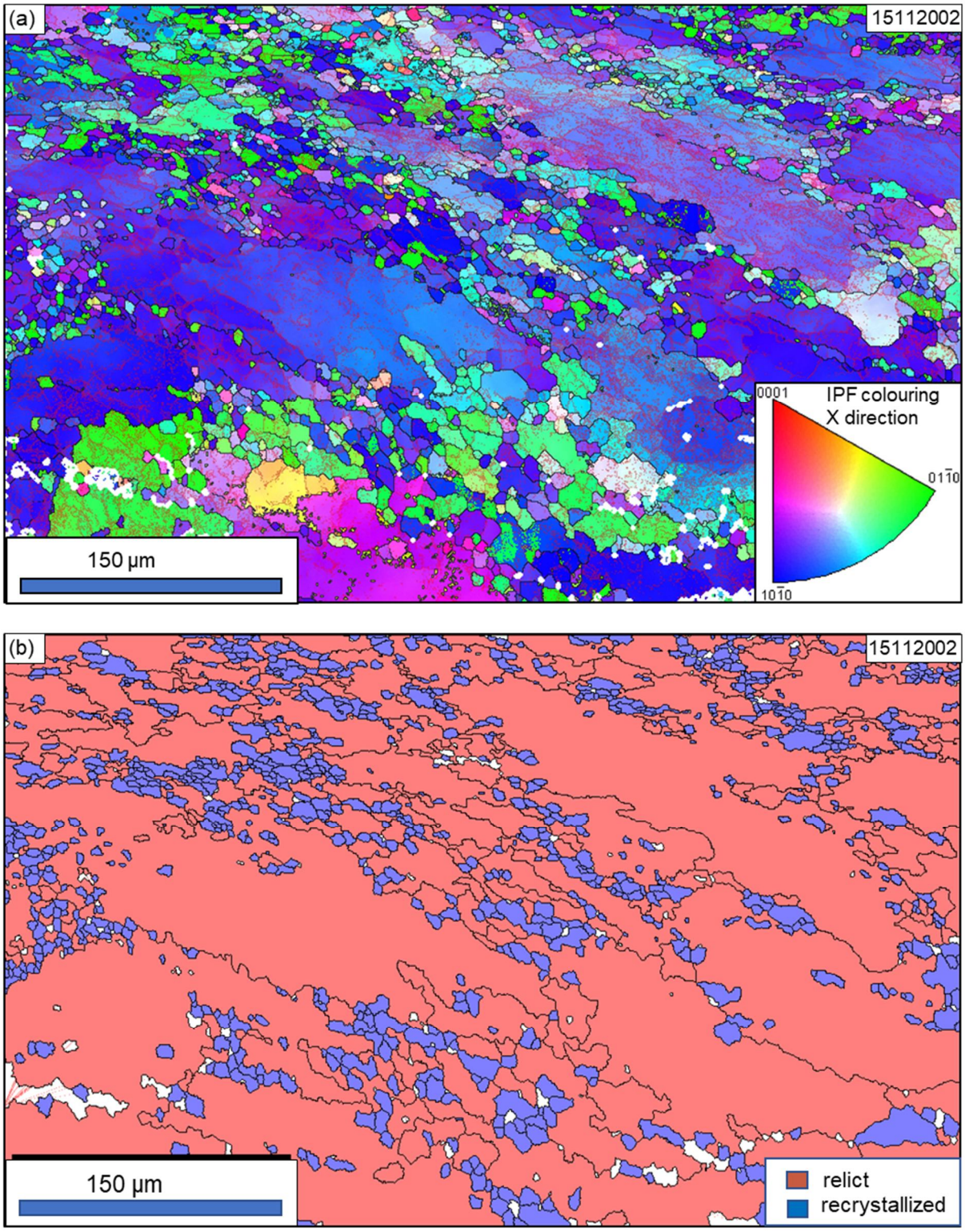

Figure 5.7. EBSD data of sample 15112002 from proto-mylonite of Area A. (a) Quartz inverse pole figure (IPF) map that was constructed by EBSD analysis. Red lines are subgrain boundaries, black lines are grain boundaries. (b)GOS-separated recrystallized and relict quartz grains map from EBSD data following Cross et al., 2017.

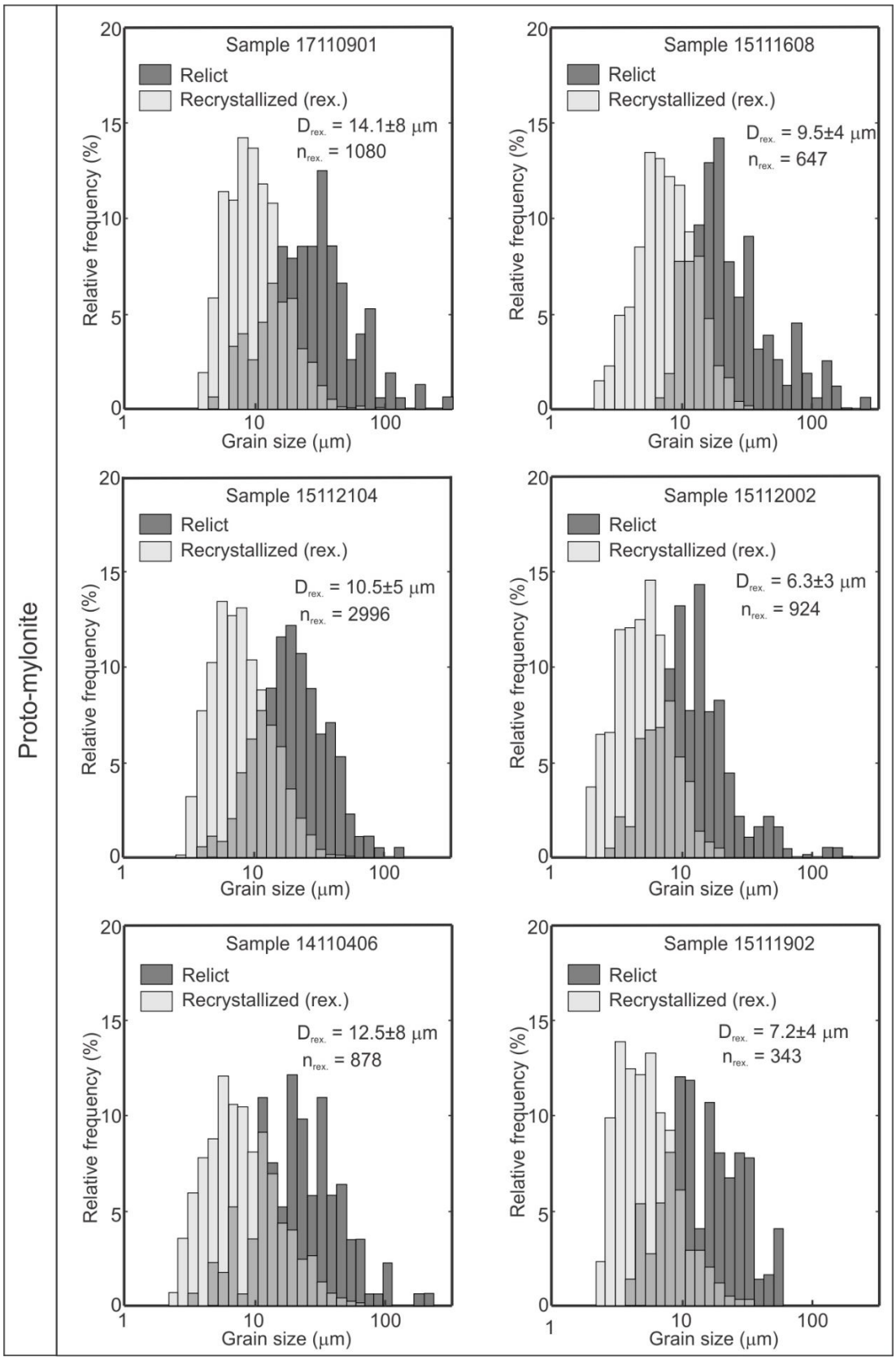

Figure 5.8. The grain size distribution of quartz which separates relict and recrystallized grain of proto-mylonite in Area A; D: root mean square of the recrystallized grain size (1 standard deviation); n number of recrystallized grains.

The distribution of quartz grains size in S-type mylonite is highly concentrated in a range 10 μm to 50 μm (e.g. samples 17110903; 1711095; 17111001; Fig. 5.11). Mean recrystallized grain sizes vary between 11.4–20 μm (Table 5.1; Fig 5.12a). The straight boundaries of recrystallized quartz grains suggest that the recrystallization occurred by SGR. In the S-type mylonite zone, the GOS threshold values are higher, varying between 4-5° (Table 1; Fig 5.12c).

The wide distribution of quartz grain size in P-type ranges between 30 μm to 1000 μm (e.g. samples 17111006; 17111007; Fig. 5.11). The recrystallized grain size of quartz varies between c. 100-120 μm (Table 1; Fig 9b, Fig 10b). Therefore, grain boundary migration recrystallization (GMB) is suggested for the mechanism of dynamic recrystallization of quartz in this zone (Stipp et al., 2002a) also considering lobate grain boundaries. The GOS threshold values increase from 2 to 4° with increasing distance from the MTL in this zone (Table 1; Fig 5.12c).

In this study, I will refer to recrystallized grain sizes of Czertowicz et al., 2019 (in press) for mylonitic samples in distance 100 m from the MTL in Tsukide region, which I have not analyzed (Table 5.1; Fig. 5.12). The range distribution of recrystallized grain size in Tsukide region form 3.6 μm of ultramylonite sample to 20.5 μm of protomylonite sample (Table 5.1).

Based on the recrystallized grain size, I use the piezometer of Cross et al. (2017), which is calibrated for use with EBSD data to estimate flow stress (Table 5.1; Fig. 5.12b). The distribution of flow stress decreases with increasing northward distance from the MTL from 250 MPa in ultramylonite sample to 22 MPa in P-type mylonite sample (Fig. 5.12b).

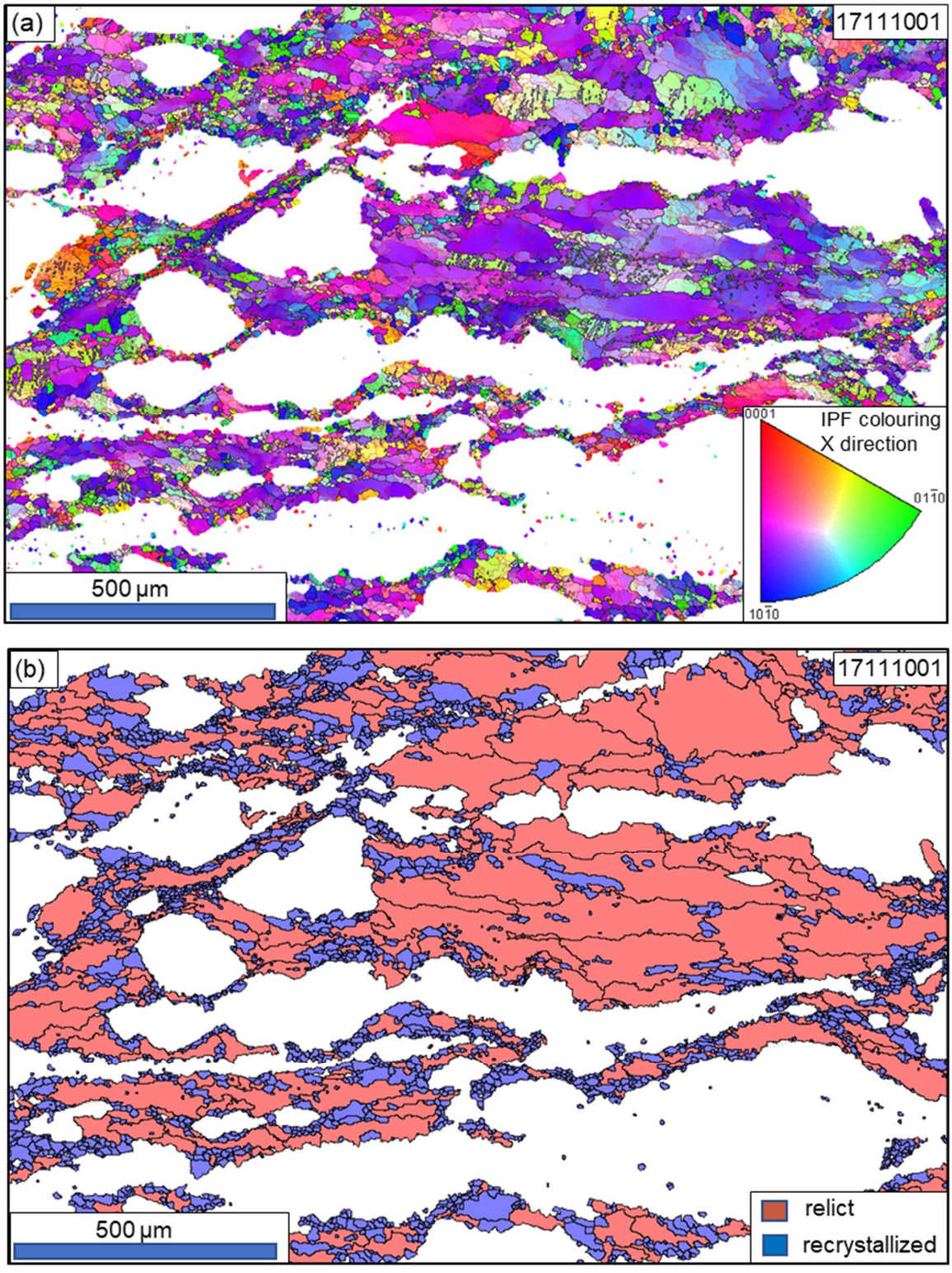

Figure 5.9. EBSD data of sample 17111001 from S-type mylonite of Area B. (a) Quartz inverse pole figure (IPF) map that was constructed by EBSD analysis. Red lines are subgrain boundaries, black lines are grain boundaries. (b) GOS-separated recrystallized and relict quartz grains map from EBSD data following Cross et al. (2017).

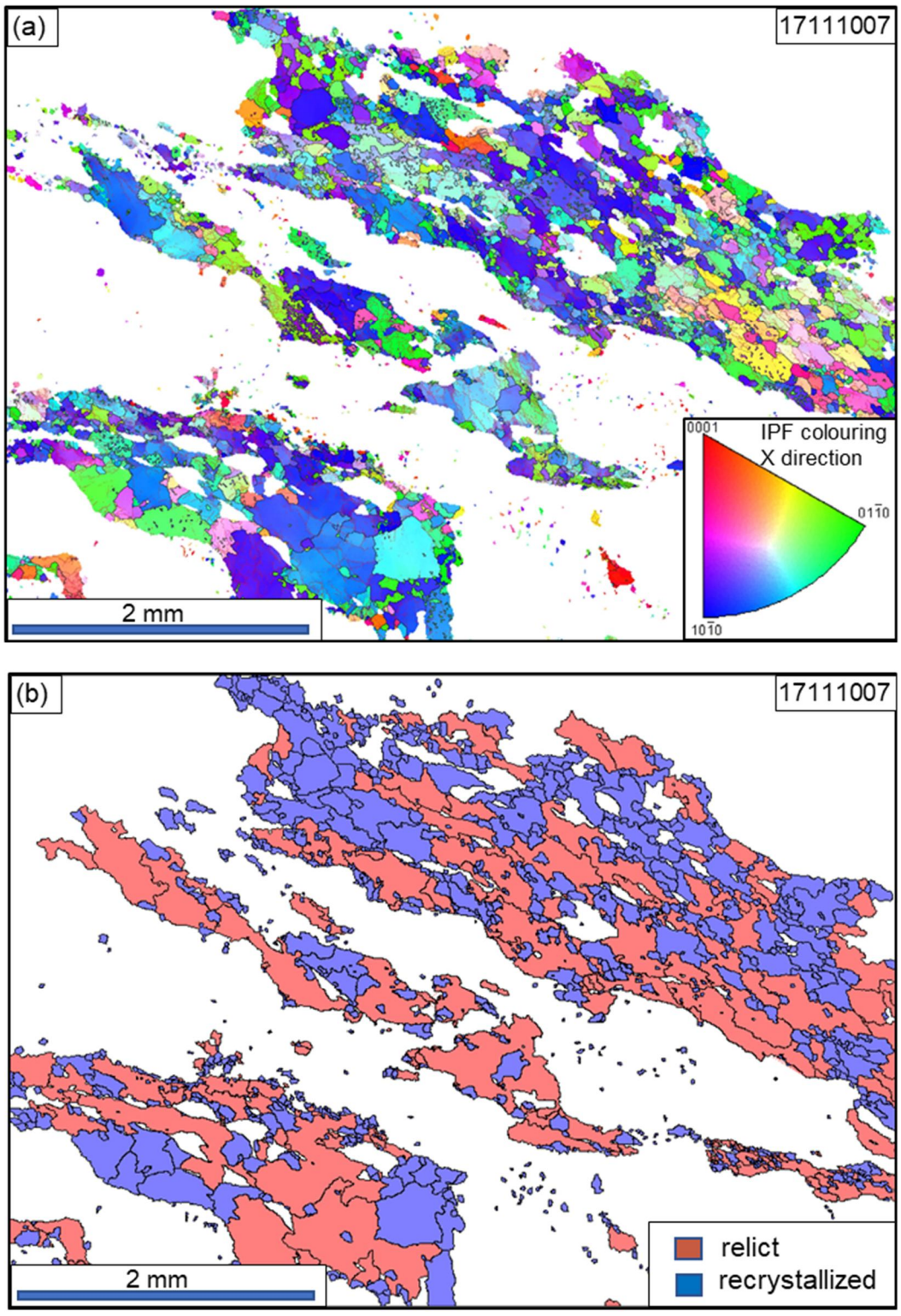

Figure 5.10. EBSD data of sample 15111608 from P-type mylonite of Area B. (a) Quartz inverse pole figure (IPF) map of that was constructed by EBSD analysis. Red lines are subgrain boundaries, black lines are grain boundaries. (b) GOS-separated recrystallized and relict quartz grains map from EBSD data following Cross et al. (2017).

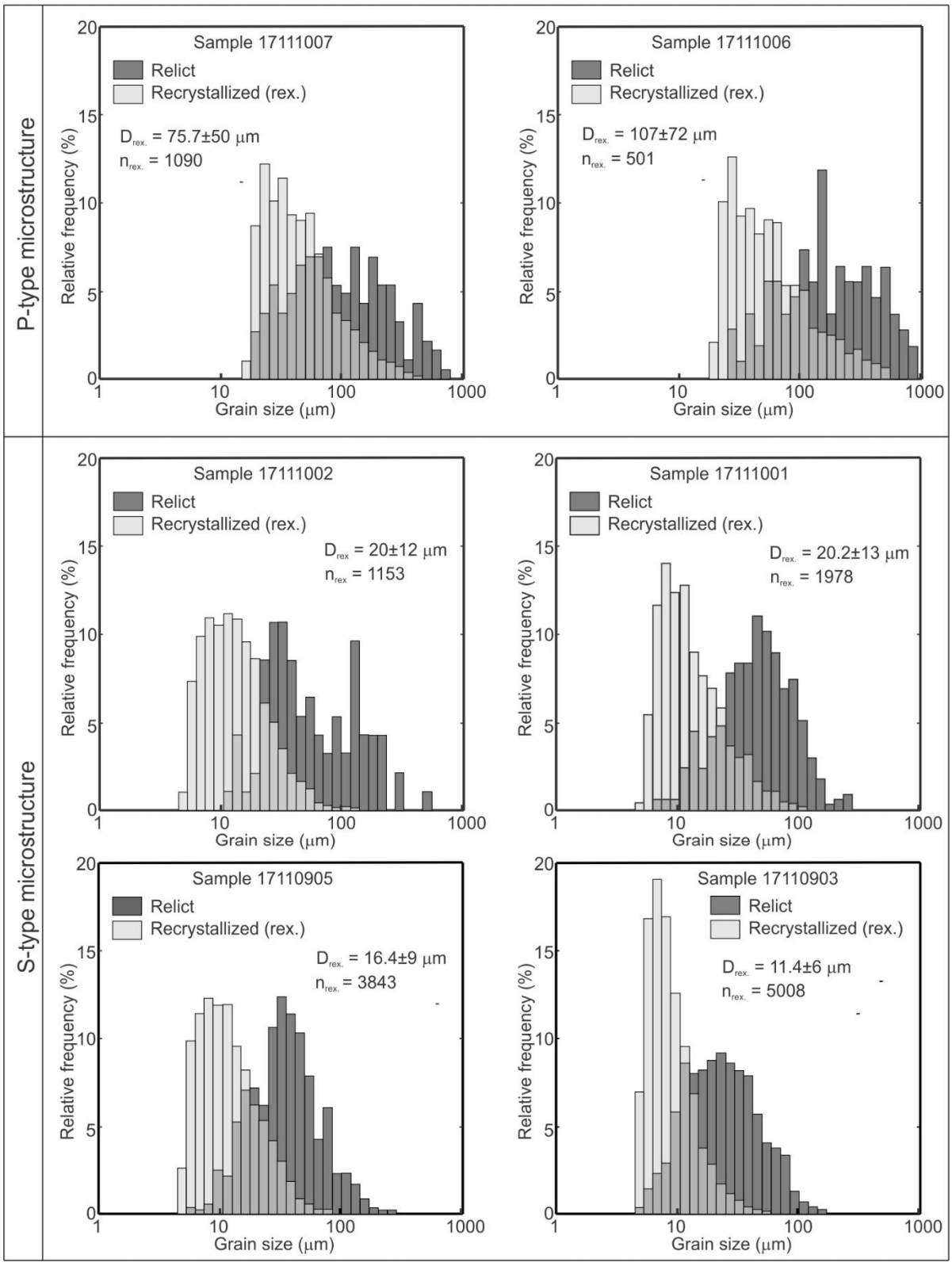

Figure 5.11. The grain size distribution of quartz which separates relict and recrystallized grain of proto-mylonite in Area B; D: root mean square of the recrystallized grain size (1 standard deviation); n number of recrystallized grains.

Table 5.1: Summary of calculated recrystallized grain size and estimate stress using the recrystallized grain size piezometer following the method of Cross et al. (2017)*

Sample No.	Northward distance from MTL (m)	Lithology	Number of Rex. grain	Rex. grain size (μm)	GOS threshold (°)	Stress (MPa)
Area A						
14110406	103	Tonalitic proto-mylonite	**878**	**12.5 ± 8**	**3**	98.9
15112002	105	Tonalitic proto-mylonite	**924**	**6.3 ± 3**	**2.3**	161.7
15111902	119	Tonalitic proto-mylonite	**343**	**7.2 ±4**	**2.9**	145.8
15111608	126	Tonalitic proto-mylonite	**647**	**9.5 ± 4**	**2.5**	120.1
15112104	132	Tonalitic proto-mylonite	**2996**	**10.5 ± 5**	**3.2**	111.9
15112106	158	Tonalitic proto-mylonite	**336**	**7.1 ± 4**	**2.5**	147.1
15111302	184	Granitic mylonite	**446**	**19.2 ± 13**	**3.2**	72.9
17110901	248	Tonalitic proto-mylonite	**1080**	**14.1 ± 8**	**3.6**	90.8
Area B						
17110903	339	Granitic mylonite	**5008**	**11.4 ± 6**	**4.3**	105.6
17111003	379	Granitic mylonite	**1005**	**19.2 ± 13**	**3.9**	72.9
17110905	421	Granitic mylonite	**2843**	**16.4 ± 9**	**4.5**	81.6
17111001	429	Granitic mylonite	**1978**	**20.2 ± 13**	**5.0**	70.3
17111002	462	Granitic mylonite	**1153**	**20.0 ± 12**	**5.3**	70.9
17111004	490	Granitic mylonite	**604**	**49.2 ± 31**	**4**	37.4
17111005	520	Granitic mylonite	**365**	**83.8 ± 63**	**2.3**	25.7
17111006	585	Granitic mylonite	**501**	**107 ± 72**	**2.6**	21.6
17111007	711	Granitic mylonite	**1090**	**75.7 ± 50**	**3.5**	27.6
Tsukide (Czertowicz at el., 2018)						
T-01	14	Ultramylonite		**6.8**	-	152.3
T-02	20	Ultramylonite		**11.2**	-	106.9
T-03	22	Mylonite		**19.2**	-	72.9
T-04	36	Protomylonite		**16.1**	-	82.6
T-05	50	Ultramylonite		**3.6**	-	239.1
T-06	78	Protomylonite		**20.5**	-	69.6

** Measurement errors in grain size is 1 standard deviation (1σ)*

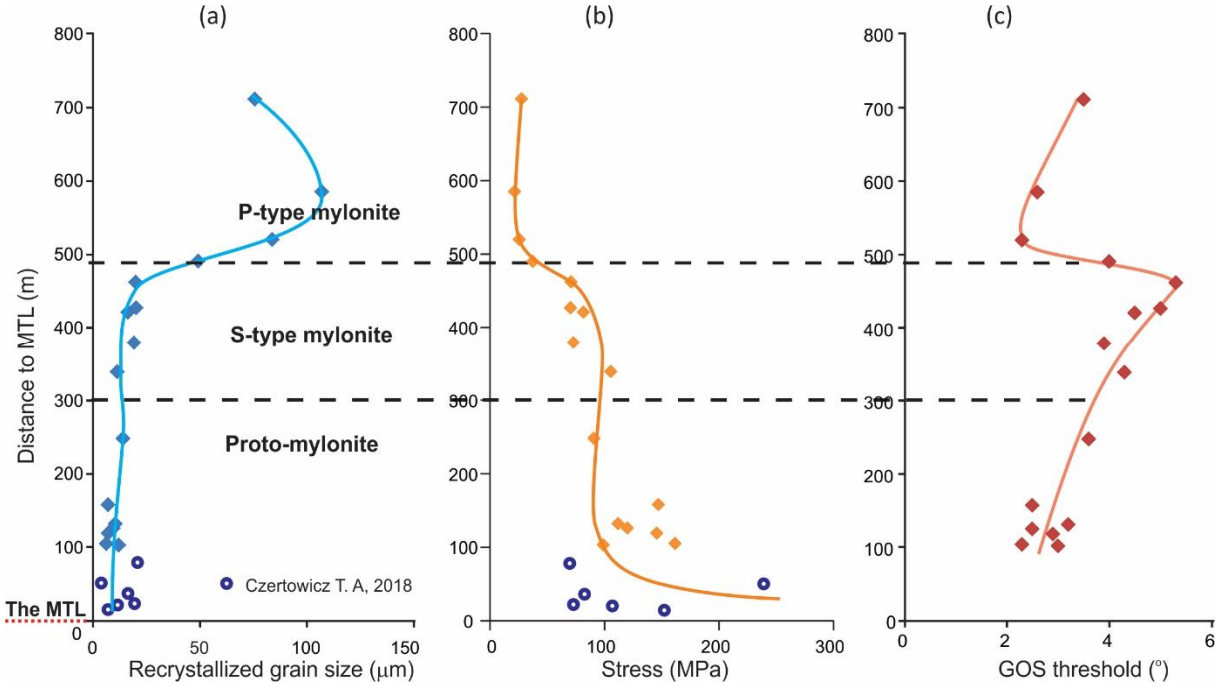

Figure 5.12. *Distribution of recrystallised grain size (a), estimated stress (b), GOS threshold values (c) for mylonitic samples plotted against the distance the MTL.*

5.1.4 Quartz crystallographic preferred orientations (CPO)

Because of the heterogeneous deformation and recrystallization in the samples, this study, I conducted the point analysis to analyze the c-axis crystallographic orientation of quartz. For each sample, 500 to 1000 points were randomly selected for quartz aggregates in the thin section. All CPO fabric plots are presented on lower hemisphere and equal area Schmidt projections.

In area A, the quartz CPOs with [c]-axes clustered parallel to the Y structural direction (Y-maximum) dominate in samples 15112002, 15112105, 15111608 and 17110901 (Fig. 5.13). However, several samples 14110406, 15111902, 15112106 show type-I crossed girdles (Schmid and Casey 1986) with c-axis maxima around 38 ° from the Y-axis on the YZ-plane, where the rhomb planes lie on the XY-plane (called R-maxima here; Fig. 5.13).

Fabric intensity of the CPOs is high (~1.5), however, is generally not correlated with distance from the MTL (Fig. 5.15a). The orientation data are plotted at the positions which tend to be closer to the Point (P) than Girdle and Random components in PGR ternary diagram (Fig. 5.15b). Only the quartz c-axis fabric in sample 15111902, where microcracks are strongly developed, shows the lowest fabric intensity and high value of the Random (R) component (Fig. 5.15a, b).

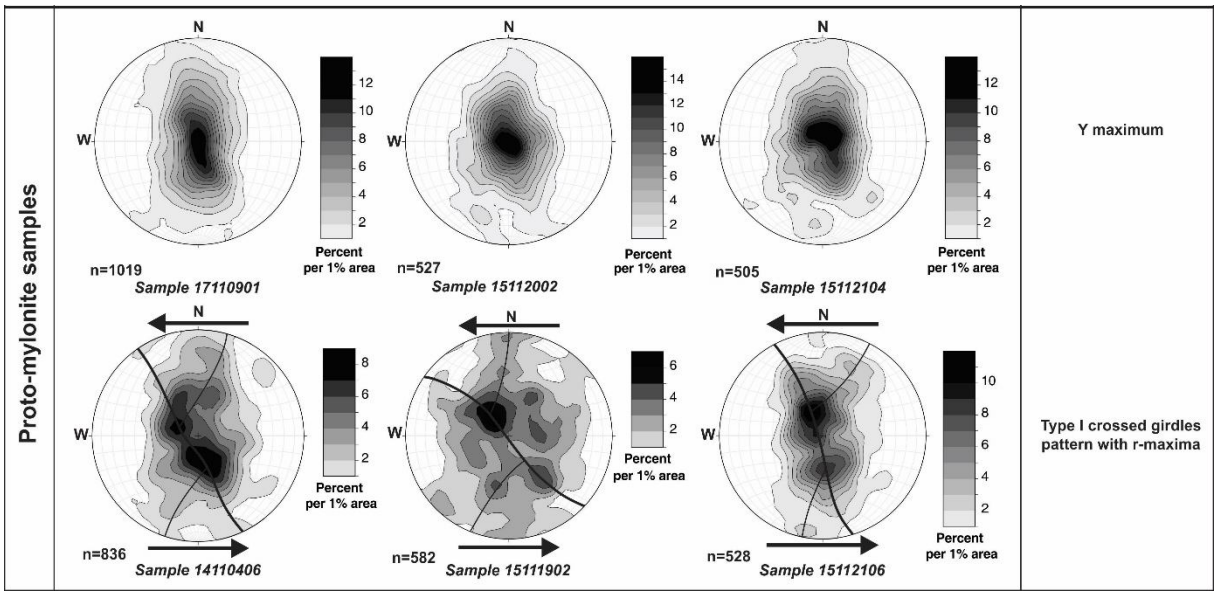

Figure 5.13. Quartz crystallographic preferred orientations data (CPO pattern) obtained from proto-mylonites of Area A. n- number of point analyzed.

In area B, the quartz CPOs with [c]-axes clustered parallel to the Y structural direction (Y-maximum) are dominant (Fig. 5.14). However, since some samples 17110903, 17111001, 17111002 in the S-type mylonite zone also show a transitional fabric between the Y-maximum and type-I crossed girdles (Fig. 5.14). Fabric intensity of the CPOs is correlated with distance from the MTL, which increases with the increasing distance from the MTL from S-type to P-type regions (Fig. 5.15a). The orientation data are plotted at the positions, which tend to be close to the Point (P) component in the PGR ternary diagram (Fig. 5.19b).

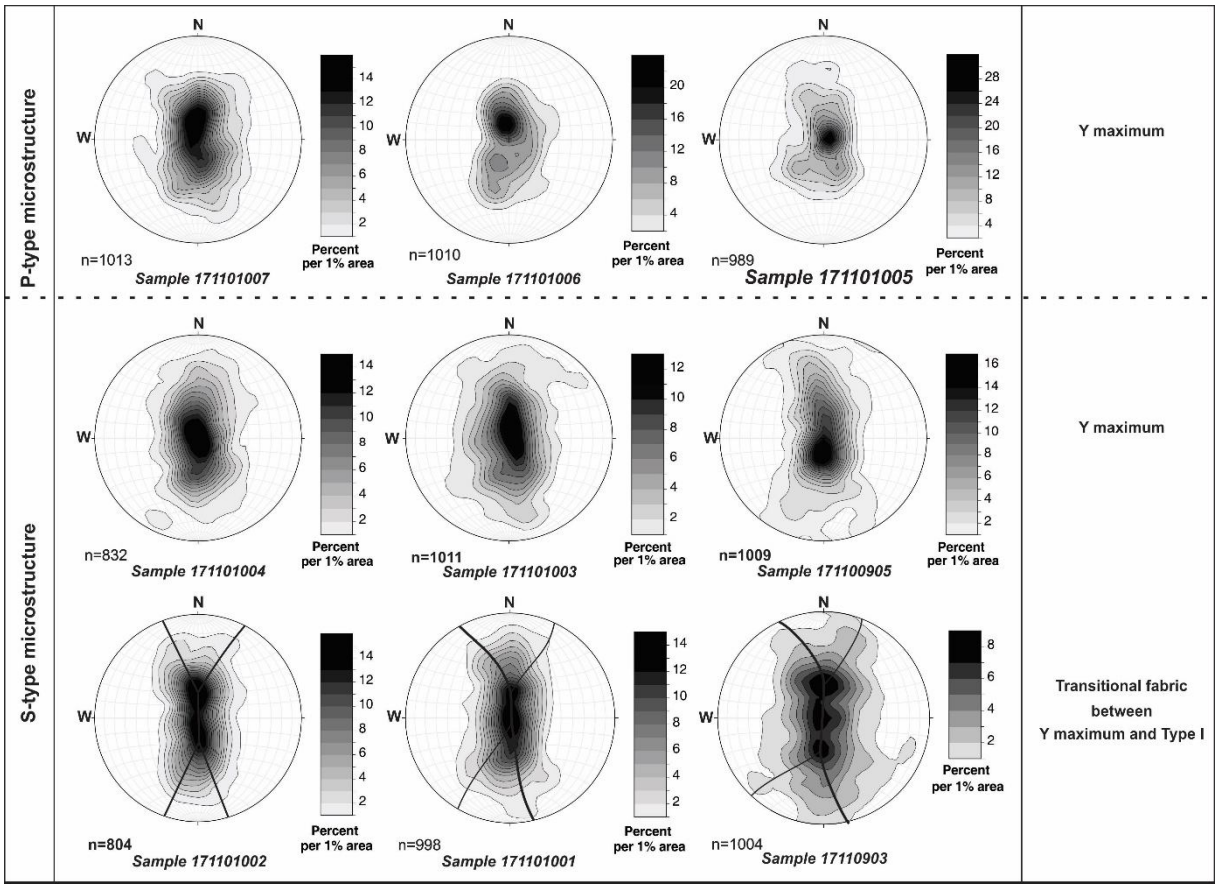

Figure 5.14. Quartz crystallographic preferred orientations data (CPO pattern) obtained from mylonites of Area B. n- number of point analyzed.

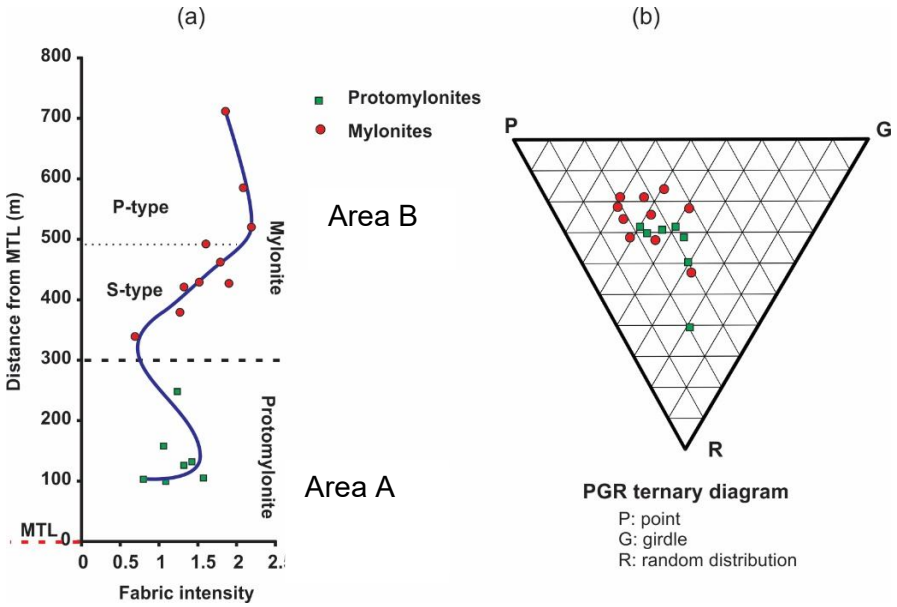

Figure 5.15. Quartz c-axis fabric strength as indicated by fabric intensity (a) and PGR ternary diagram (b) in the area A and area B. $P = \lambda_1 - \lambda_2$, $G = 2(\lambda_2 - \lambda_3)$, $R = 3\lambda_3$, where λ_n represent the eigenvalues of the normalized orientation tensor (Vollmer 1990).

Table 5.2. Summary of pattern, strength and the orientation data trend of quartz c-axis fabric.

Sample No.	Distance from MTL (m)	Microstructure	Quartz CPO pattern	Intensity (Fi)	Point (P)	Girdle (G)	Random (R)
Area A							
14110406	103	Proto-mylonite	Type-I & R-maximum	0.799	0.303	0.300	0.397
15112002	105	Proto-mylonite	Y-maximum	1.575	0.498	0.221	0.281
15111902	119	Proto-mylonite	Type-I & R-maximum	0.329	0.188	0.208	0.604
15111608	126	Proto-mylonite	Y-maximum	1.323	0.431	0.278	0.291
15112104	132	Proto-mylonite	Y-maximum	1.427	0.467	0.23	0.303
15112106	158	Proto-mylonite	Type-I & R-maximum	1.062	0.357	0.327	0.316
17110901	248	Proto-mylonite	Y-maximum	1.238	0.398	0.320	0.282
Area B							
17110903	339	S-type mylonite	Transition between Y-maximum & Type-I	0.694	0.276	0.294	0.430
17111003	379	S-type mylonite	Y-maximum	1.272	0.433	0.243	0.324
17110905	421	S-type mylonite	Y-maximum	1.325	0.390	0.388	0.223
17111001	429	S-type mylonite	Transition between Y-maximum & Type-I	0.1903	0.536	0.278	0.186
17111002	462	S-type mylonite	Transition between Y-maximum & Type-I	1.793	0.493	0.347	0.160
17111004	462	P-type mylonite	Y-maximum	1.608	0.487	0.270	0.242
17111005	520	P-type mylonite	Y-maximum	2.195	0.603	0.211	0.196
17111006	585	P-type mylonite	Y-maximum	2.089	0.594	0.188	0.218
17111007	711	P-type mylonite	Y-maximum	1.859	0.558	0.186	0.256
Tsukide (Czertowicz, 2018**)**							
T-01	14	Ultramylonite	Type-I & R-maximum	-	-	-	-
T-02	20	Ultramylonite	Type-I & R-maximum	-	-	-	-
T-03	22	Mylonite	Random & R-maximum	-	-	-	-
T-04	36	Protomylonite	Z-maximum	-	-	-	-
T-05	50	Ultramylonite	Random & Y-maximum	-	-	-	-
T-06	78	Protomylonite	Y-maximum & single girdle	-	-	-	-

5.2 Feldspar microstructures

Not only quartz microstructure, but also feldspar microstructures variation in the shear zone is investigated in the present study. In area A, K-feldspar is absent, and plagioclase porphyroclasts are less deformed. In plagioclase porphyroclasts from several

samples, microcracks are developed (Fig. 3.3a; 5.17a).

Whereas in area B, K-feldspar is rich and strongly deformed. In samples 17110903, 17110905, 17111003, 17111001 showing S-type quartz microstructures, some K-feldspar porphyroclasts are elongated and flattened by microcracking (Fig. 5.17b). In samples 17111001, 17111002 with the very high aspect ratio in quartz, large K-feldspar phorphyroclasts become rounded and surrounded by the layer consisting of the smaller plagioclase grains (Fig. 3.4b). Whereas in P-type mylonite, K-feldspar porphyroclasts show an elongated ribbon (Fig. 5.17c) or fish shape (Fig. 5.17d).

Moreover, K-feldspar porphyroclast is replaced by myrmekite, plagioclase-and vermicular quartz symplectite at the side perpendicular to the compression direction (Simpson 1985; Simpson & Wintsch 1989; Vernon 1992) (Fig. 5.16a). Some K-feldspar porphyroclasts show perthite structure is characterized by the intergrowth of sodic and potassic feldspar resulting from subsolidus exsolution (Fig. 5.16b).

Figure 5.18 shows the temperatures which are calculated from the compositional data of coexisting plagioclase and K-feldspar (Table 5.3) for mylonite samples in Area B based on the thermometer after Stormer (1975) and Stormer and Whitney (1985). For calculation, I assume that the compositions of plagioclase and K-feldspar in the myrmekite structures are in equilibrium and the pressure during the formation of myrmekite is 300 MPa equivalent to the depth of c. 10 km. Deformation temperatures for mylonites showing S-type quartz microstructure are 350–450°C and for mylonites showing P-type quartz microstructure are 420–520°C.

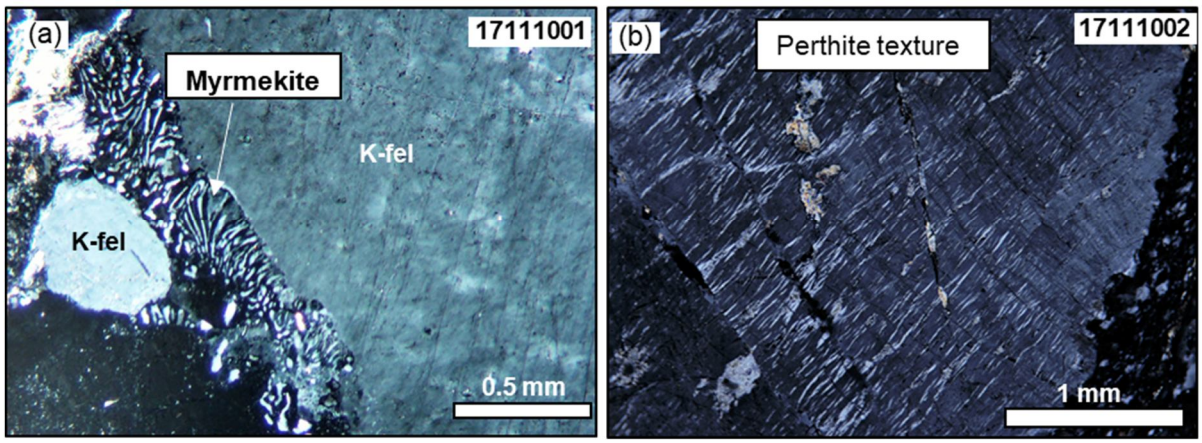

Figure 5.16. Photomicrographs (crossed polarized) of microstructural observations in K-feldspar from mylonite of Area B. (a) Occurrence of myrmekite indicate the replacement of K-feldspar by plagioclase and quartz at greenschist facies or amphibolite facies. (b) Perthitic texture.

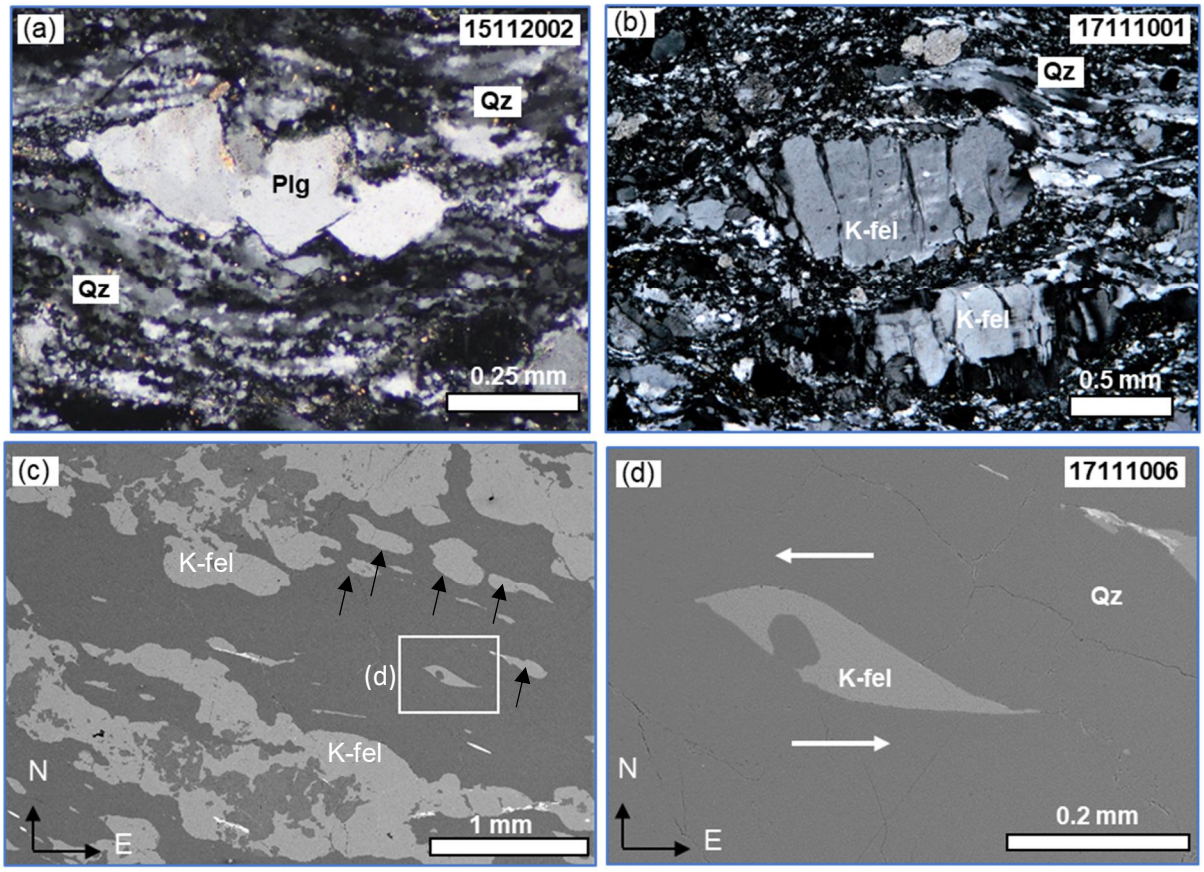

Figure 5.17. Feldspar microstructures. Fracture in plagioclase porphyroclast in proto-mylonite (a) and K-feldspar in mylonite (b) representing britlle deformation. (c) Back-scatter electron image showing elongated K-feldspar grains (black arrow) suggesting ductile deformation in high-grade of P-type mylonite. (d) a fish shaped K-feldspar grain (white box in Fig. c) indicating a top to the west shear sense.

Table 5.3: Composition of a pair of two feldspars and temperature data obtained from two feldspar thermometry.

	Alkali feldspars			Plagioclase				
Sample	**An (wt.%)**	**Ab (wt.%)**	**Or (wt.%)**	**An (wt.%)**	**Ab (wt.%)**	**Or (wt.%)**	**T1 (°C)**	**T2 (°C)**
17111007(1)	0.00	0.10	0.90	0.13	0.86	0.01	436.09	483.79
17111007(5)	0.00	0.11	0.89	0.11	0.88	0.01	442.92	491.55
17111007(6)	0.00	0.13	0.87	0.13	0.86	0.01	465.87	516.16
17111006(1)	0.00	0.09	0.91	0.08	0.92	0.01	403.20	450.45
17111006(3)	0.00	0.07	0.93	0.11	0.88	0.01	388.42	435.02
17111006(5)	0.00	0.09	0.91	0.12	0.87	0.01	410.29	457.11
17111005(1)	0.00	0.08	0.92	0.01	0.99	0.00	379.54	427.07
17111005(2)	0.00	0.06	0.94	0.01	0.99	0.00	355.91	403.43
17111005(3)	0.00	0.12	0.88	0.06	0.93	0.01	437.50	486.90
17111004(1)	0.00	0.07	0.93	0.25	0.73	0.02	398.22	443.11
17111004(2)	0.00	0.06	0.93	0.13	0.85	0.02	371.46	417.68
17111004(3)	0.00	0.06	0.94	0.25	0.71	0.03	383.19	428.13
17111003(4)	0.00	0.04	0.95	0.12	0.87	0.01	327.00	374.25
17111003(5)	0.00	0.03	0.97	0.11	0.88	0.01	286.53	335.24
17111003(6)	0.00	0.04	0.96	0.04	0.91	0.06	306.65	354.65
17111002(1)	0.00	0.06	0.94	0.24	0.75	0.01	384.98	430.23
17111002(2)	0.00	0.03	0.97	0.14	0.82	0.04	302.97	350.97
17111002(5)	0.00	0.06	0.94	0.21	0.79	0.01	368.10	413.89
17111001(1)	0.00	0.06	0.94	0.18	0.80	0.02	373.19	419.35
17111001(2)	0.00	0.06	0.94	0.14	0.85	0.02	368.20	414.74
17111001(4)	0.00	0.04	0.96	0.16	0.83	0.01	324.19	371.93
17110903(1)	0.00	0.04	0.96	0.16	0.83	0.02	320.65	367.99
17110903(1)	0.00	0.05	0.95	0.14	0.84	0.02	338.51	385.31
17110903(1)	0.00	0.03	0.97	0.17	0.83	0.01	299.32	347.47

T1: After Stormer, 1975 T2: After Stormer and Whitney, 1985

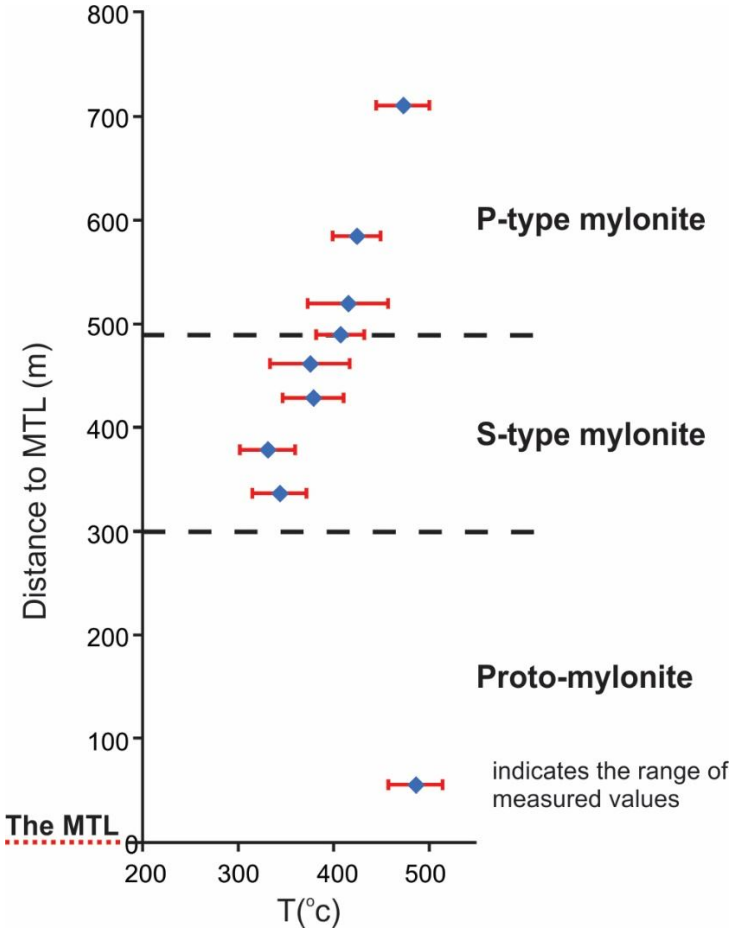

Figure 5.18 Plotting of the results from two-feldspar thermometer against the distance from the MTL.

5.4 Dislocation substructures of quartz

According to the volume fraction and microstructures of recrystallized grains the quartz microstructures within the MTL shear zones in the Tsukide region can be grouped into five types, here referred to as type A to E. Type A microstructure is observed in quartz relict grains from the protomylonite samples characterized by strong plastic deformation. Type B microstructure is observed in recrystallized grains from the protomylonite samples characterized by complete recrystallization and occurrence of static recrystallization in some domains. Type C and type D microstructure are observed in quartz relict and recrystallized grains with S-type microstructures (Masuda, and Fujimura, 1981), respectively, which are both very strongly plastically deformed. Type E microstructure is observed in recrystallized quartz grains with P-type microstructures (Masuda, and Fujimura, 1981) that were formed by the GBM dynamic recrystallization. In this section, first, the overall characteristics of type A to E microstructures are described.

5.4.1. Type A microstructure

Type A microstructure is observed in quartz relict grains from the protomylonite samples in the Area A (Fig. 3.1) of the area study. Some of the quartz grains occur as large (Fig. 3a), highly flattened relict grains, showing patchy and undulose extinction, and deformation lamellae (Fig. 5.2a). The highly heterogeneous type A quartz microstructure is also shown in heterogeneous submicroscopic dislocation structures observed under a TEM (Fig. 5.19). Most conspicuous microstructures at the submicroscopic scale observed under a TEM are elongate subgrains with straight and curved, parallel low angle grain boundaries (Fig 5.19 a, b). The subgrains are folded in the fig. 5.19a showing kink bands. The subgrains are created by subboundaries (Fig. 5.19 d), and in some area dislocation networks occur (Fig. 5.19 e). Fluid inclusions occur along both subgrain boundaries (Fig.5.19 b) and grain boundaries, and intragranular fluid inclusions also occur (Fig. 5.19 f). The free dislocation density varies within one order of magnitude between about $2x10^8$ cm^{-2} and $10x10^8$ cm^{-2} (Fig. 5.24 a). Most of the dislocations lie on the rhomb and prism planes, and less frequently on the basal plane of quartz.

5.4.2. Type B microstructure

Type B microstructure is observed in recrystallized grains from the protomylonite samples with the size less than 10 μm. Small recrystallized grains with straight or simply curved grain boundaries with few dislocations are observed under a TEM (Fig. 5.20). Also, a typical foam structure with straight or simply curved grain boundaries meeting at c. 120° angles at the grain edges is conspicuous under a TEM. The free dislocation density varies within one order of magnitude between about $4x10^7$ cm^{-2} and $2.3x10^8$ cm^{-2} (Fig. 5.24 b). Fluid inclusions (Fig. 5.20 a, c) occur along both subgrain and grain boundaries but intragranular fluid inclusions are not observed.

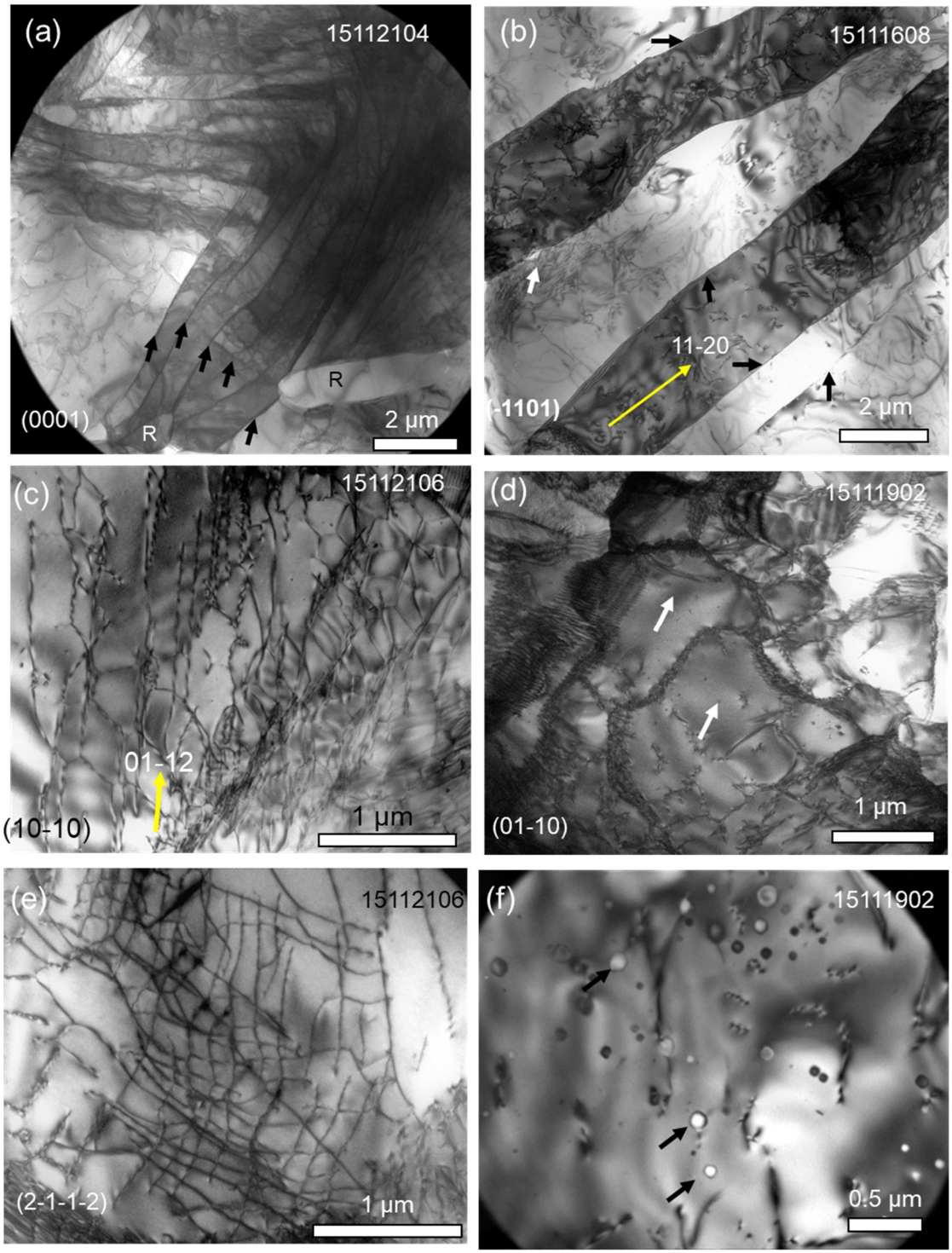

Figure 5.19. TEM bright-field micrographs of the type A quartz microstructure from the quartz relict grains in the protomylonite. (a) Curved and folded subboundaries (black arrows) and elongated recrystallized grains (R). (b) Straight parallel subboundaries (black arrow) decorated with fluid inclusions (white arrow). (c) dislocation line and dislocation network (d) subgrains are created by subboundaries (e) Dislocation networks. (f) intragranular fluid inclusions.

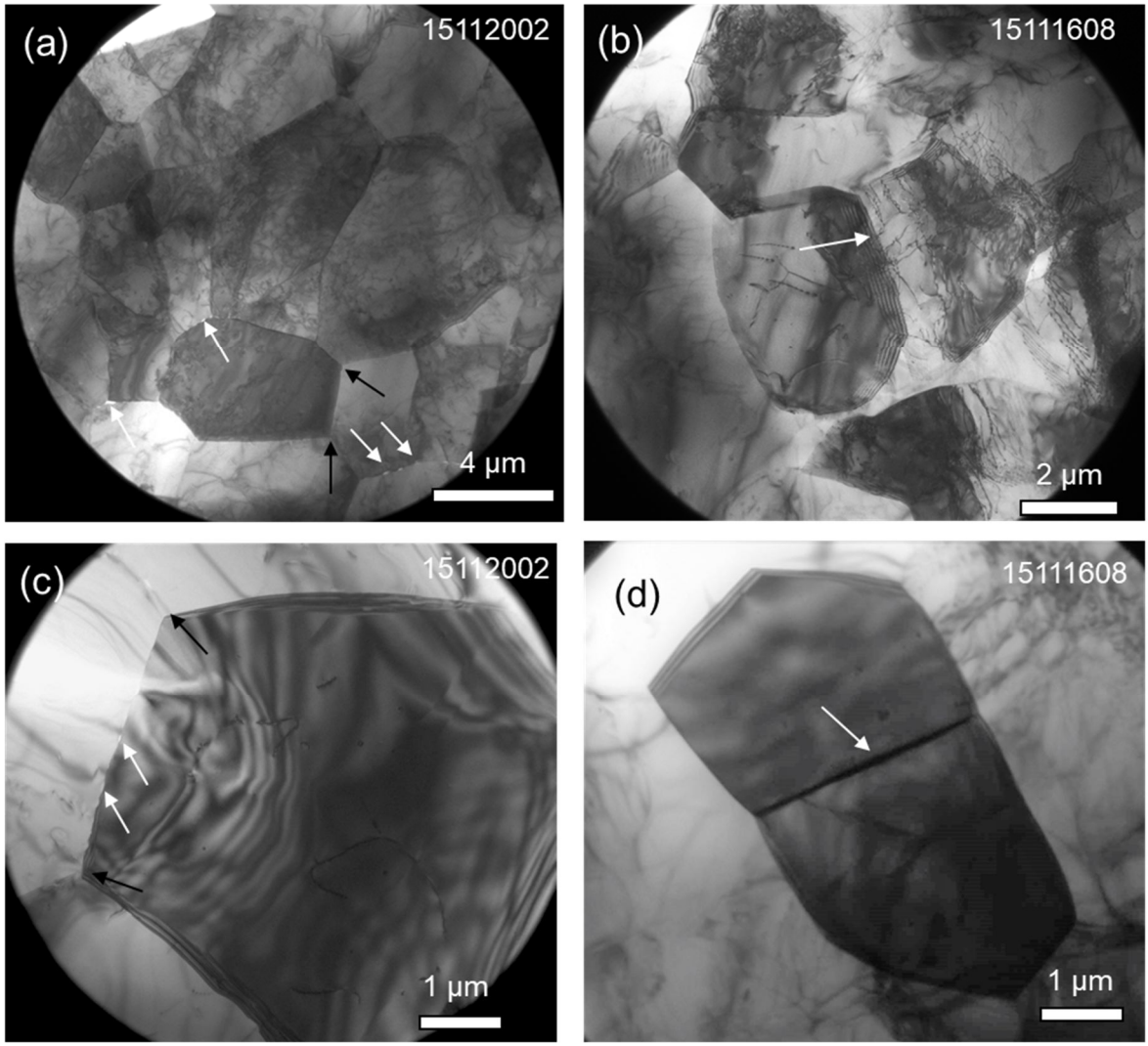

Figure 5.20. *TEM bright-field micrographs of the type B quartz microstructure from the recrystallized grains in the protomylonite. (a) Recrystallized grains with typical 120° angles between the boundaries at grain edges (black arrow) and grain boundaries decorated with fluid inclusions (white arrow). (b) Recrystallized grains with subgrain boundaries (white arrow). (c) Recrystallized grains with typical 120° angles between the boundaries at grain edges (black arrow) and grain boundaries decorated with fluid inclusions (white arrow). (d) Recrystallized grains with subgrain boundaries (white arrow).*

5.4.3. Type C microstructure

Type C microstructure is observed in strongly elongated S-type relict grains. The highly heterogeneous type C quartz microstructure reveals a heterogeneous submicroscopic structure under TEM (Fig. 5.21) similar to the one observed under a petrographic microscope. There are numerous occurrences of dislocation that form the

subgrain boundaries (Fig. 5.21 a, b,c). Also, some domains, the free dislocation density is very high (Fig. 5.21 d), which varies within one order of magnitude between about $1x10^8$ cm^{-2} and $14x10^8$ cm^{-2} (Fig. 5.24 c). A grain boundary is curved (Fig. 5.21 e) and bulged (Fig. 5.27 f) indicating BLG recrystallization. Fluid inclusions occur along both subgrain boundaries and grain boundaries. Most of the dislocations lie on the basal and rhomb planes of the quartz.

5.4.4. Type D microstructure

Type D microstructure is observed recrystallized quartz grains with the size about 20 μm and S-type microstructures. New elongate grains with high and homogeneous dislocation densities are observed under a TEM (Fig. 5.22). The free dislocation density varies within one order of magnitude between about $5x10^7$ cm^{-2} and $2.9x10^8$ cm^{-2} (Fig. 5.24 d). Fluid inclusions (Fig. 5.22 a, c) occur along both subgrain and grain boundaries but intragranular fluid inclusions are not observed.

5.4.5. Type E microstructure

Type E microstructure is observed in recrystallized quartz grains with P-type microstructures that are formed by GBM dynamic recrystallization. The highly heterogeneous type E quartz dislocation microstructure is observed by the TEM (Fig. 5.23). Strongly curved grain boundaries (Fig. 5.23 b, c) are perhaps created by GBM recrystallization. The free dislocation density varies within one order of magnitude between about $1x10^8$ cm^{-2} and $8x10^8$ cm^{-2} (Fig. 5.24 e). Fluid inclusions (Fig. 5.23b) occur along both subgrain and grain boundaries.

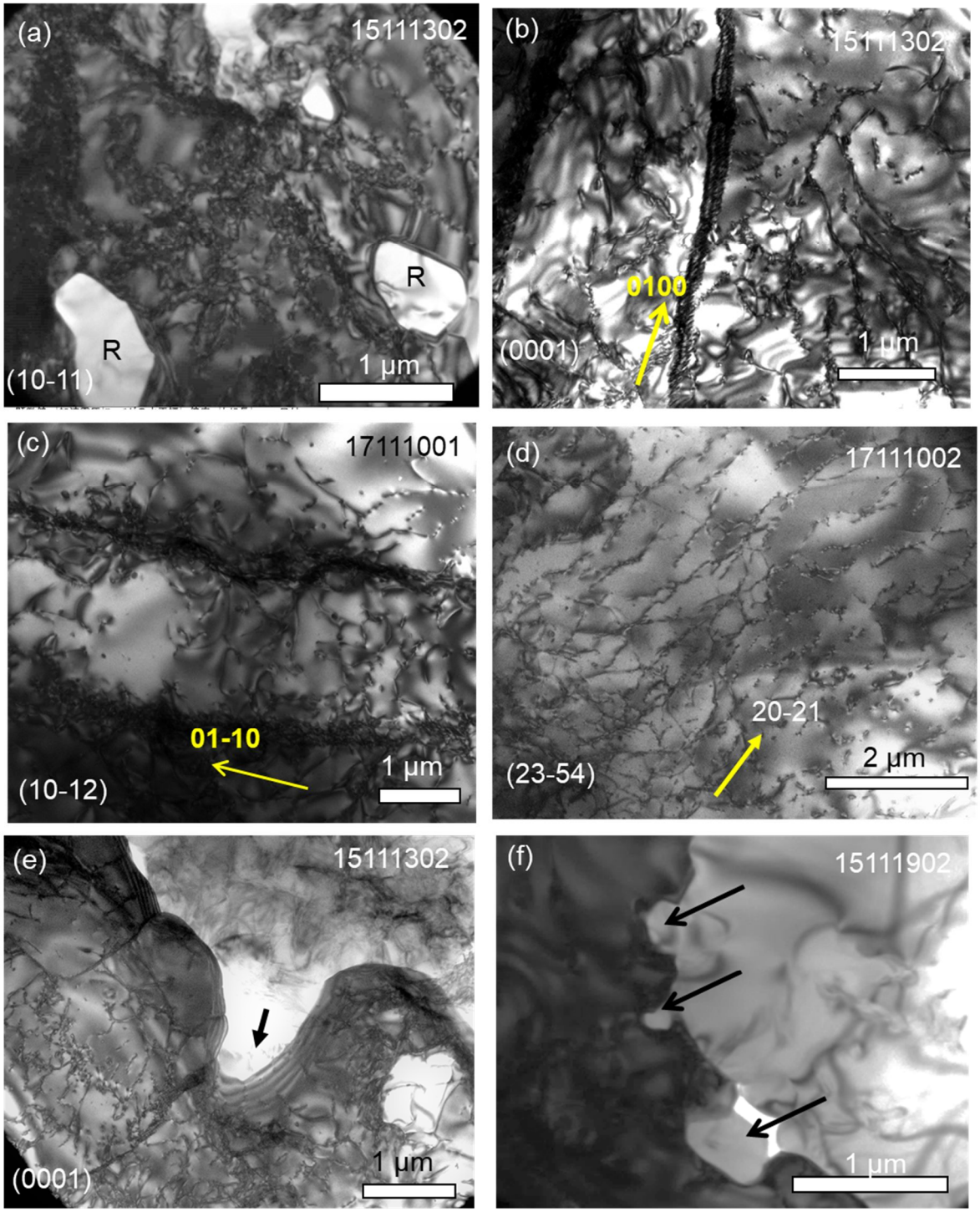

Figure 5.21. *TEM bright-field micrographs of the type C quartz microstructure from the recrystallized grains in the S- type mylonite samples. (a, b, c) Dislocation tangle created the low angle grain boundaries. (d) High free dislocation density and tangle dislocation. (e) Grain boundary curved. (f) Grain boundary bulged.*

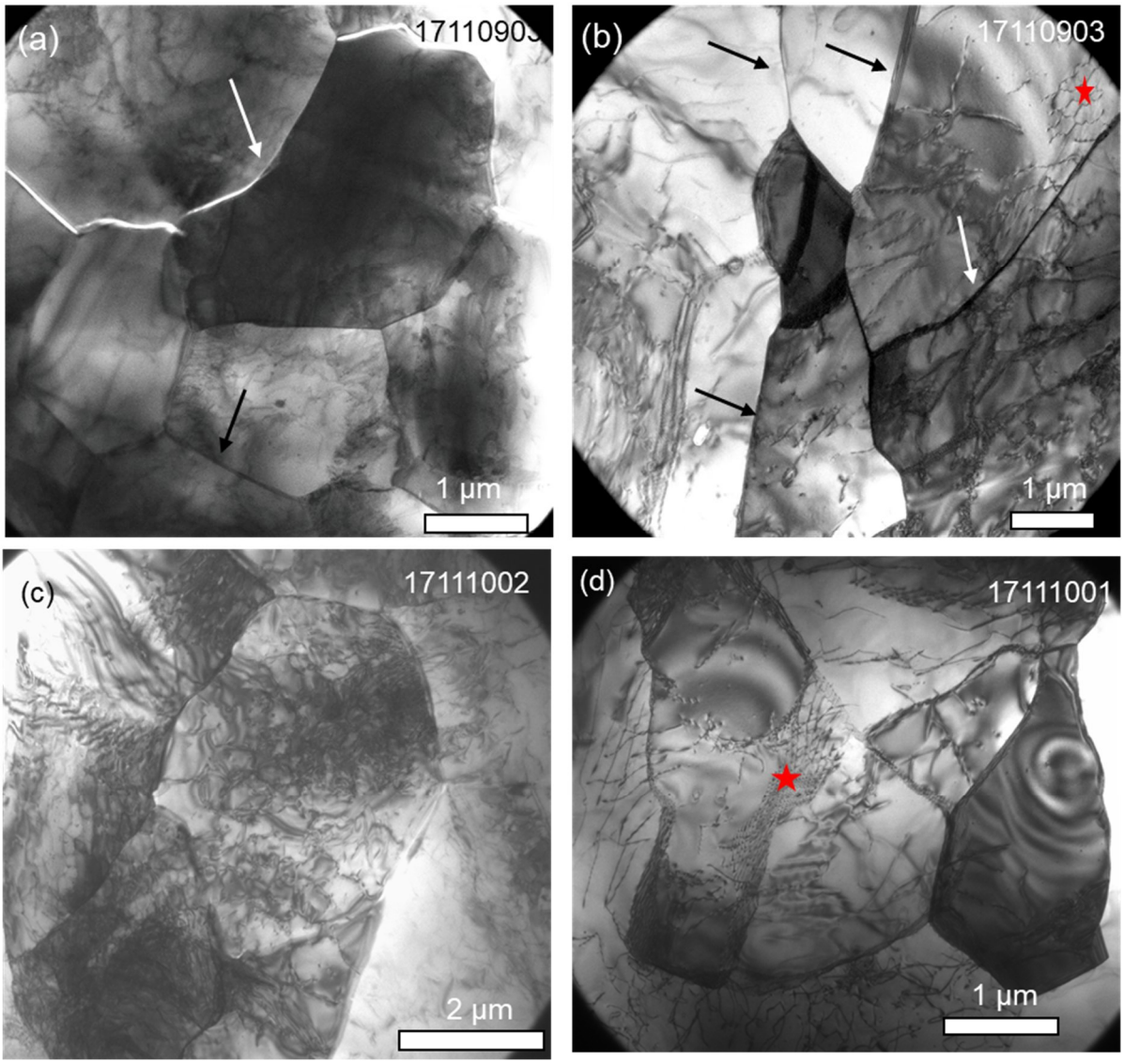

Figure 5.22. *TEM bright-field micrographs of the type D quartz microstructure from the recrystallized grains in the S- type mylonite samples. New elongate grains with high and homogeneous dislocation density. (a) Smoothly curved recrystallized grain boundaries (white arrow) and straight recrystallized grain boundaries (black arrow). (b) elongated recrystallized grains with straight boundaries and curved subgrain boundaries (white arrow), and hexagonal networks of screw <a> dislocations in the basal plane (red star). (c) Very high dislocation densities in the subgrains. (d) dislocation networks (red star).*

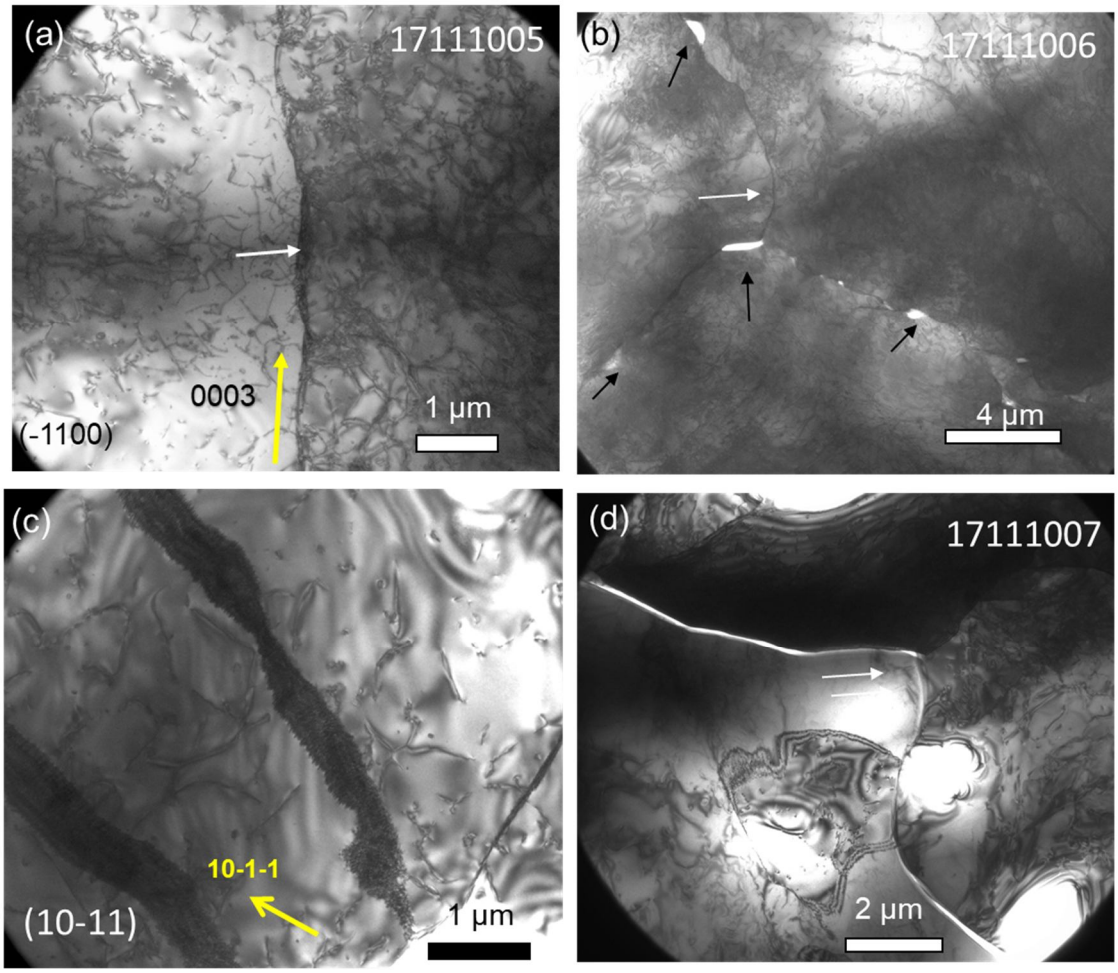

Figure 5.23. *TEM bright-field micrographs of the type E quartz microstructure from the recrystallized grains in the P-type mylonite. (a, c) Curved subgrain boundaries. (b, d) Curved grain boundaries (white arrow) indicating GBM are decorated with fluid inclusions (black arrow).*

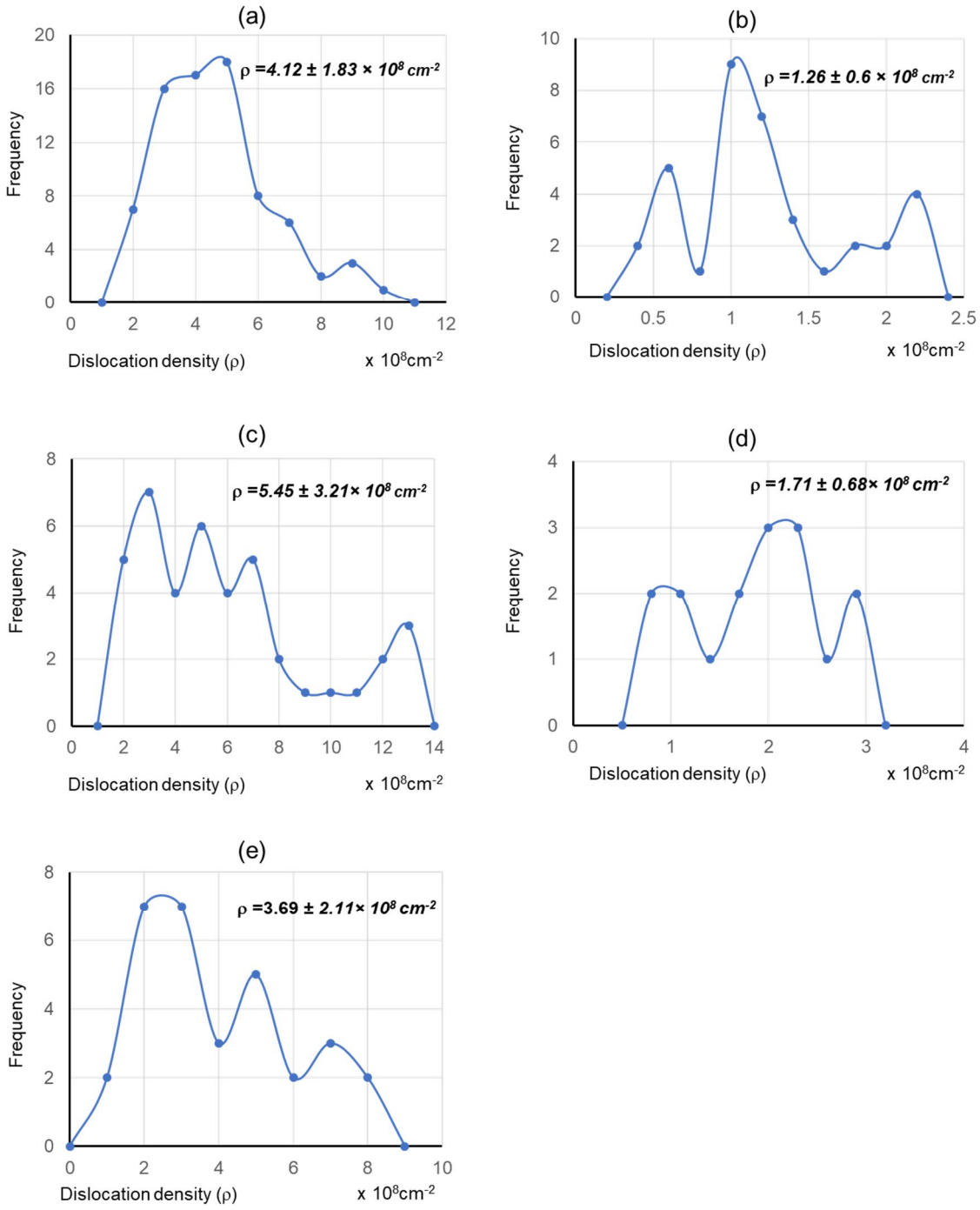

Figure 5.24. *The Dislocation density in the quartz aggregate in the mylonite samples from the MTL.*

The average of dislocation density which calculated for each submicrostructure shows high dislocation density in S-type mylonite microstructure ($\rho = 5.45 \pm 3.21 \times 10^8$ cm^{-2}), lower dislocation density in protomylonite ($\rho = 4.12 \pm 1.83 \times 10^8$ cm^{-2}) and P-type mylonite microstructure ($\rho = 3.69 \pm 2.11 \times 10^8$ cm^{-2}) (Table 5.4). In small recrystallized grains the dislocation density is low with $\rho = 1.26 \pm 0.6 \times 10^8$ cm^{-2} in proto-mylonite

zone and $\rho = 1.71 \pm 0.68 \times 10^8$ cm^{-2} in S-type mylonite microstructure. Flow stresses (MPa) which are calculated from dislocation densities following by McCormick, (1977) are also shown in Table 5.4.

Table 5.4 Summary of flow stresses (MPa) which are calculated from dislocation densities following McCormick, (1977) in prtomylonite and mylonite samples.

Type of microstructure	**Average ρ (cm^{-2})**	**Stressσ (MPa)**
Type A	$4.12 \pm 1.83 \times 10^8$	80.69
Type B	$1.26 \pm 0.6 \times 10^8$	36.40
Type C	$5.45 \pm 3.21 \times 10^8$	95.69
Type D	$1.71 \pm 0.68 \times 10^8$	44.53
Type E	$3.69 \pm 2.11 \times 10^8$	73.97

6. Discussion

6.1. Deformation temperature of fault rocks along the MTL

Microstructures and crystallographic preferred orientations (CPOs) of quartz are often used to infer deformation temperatures and mechanisms that operated in ancient shear zones (Schmid and Casey 1986; Hirth and Tullis 1992; Passchier and Trouw 1998; Takeshita et al. 1999; Stipp et al. 2002; Little et al. 2013).

Dynamic recrystallization could occur by progressive rotation of subgrains or grain boundary migration (e.g. Guillope & Poirier, 1979; Urai et al, 1986). It has been found that one of the following three mechanisms of dynamic recrystallization becomes dominant in deformed quartz with increasing temperature (Stipp et al, 2002). These are termed bulging (BLG; e.g. Drury et al, 1985), subgrain rotation (SGR; e.g. Hobbs, 1968; White, 1973; Guillope & Poirier, 1979) and grain boundary migration (GBM; e.g. Guillope & Poirier, 1979; Urai et al, 198,) recrystallization, respectively. At low-temperature conditions, the BLG recrystallization occurs where local grain boundary migration is the dominant process (Stipp et al, 2002). With increasing temperature, subgrain rotation recrystallization becomes dominant. At more higher temperature conditions above the temperature range of SGR, the dominant recrystallization mechanism is GBM (Guillope & Poirier, 1979; Urai et al, 1986).

In an experimental study, three dislocations creep regimes for quartz have been identified by Hirth & Tullis (1992) based on mechanical data and recrystallization mechanisms identified by TEM and light microscope observations. Hirth & Tullis (1992) have demonstrated that the dominant recrystallization mechanism is controlled by temperature, stress and strain rate. In regime 1, recrystallization is mainly accommodated by strain-induced grain boundary migration, in regime 2 by climb-controlled dislocation creep (subgrain rotation) and in regime 3 by both grain boundary migration and subgrain rotation (Hirth & Tullis, 1992).

In a study on naturally deformed quartz from the Eastern Tonale fault by Stipp et al. (2002), the whole range of natural dynamic recrystallization microstructures of quartz can be observed within a single shear zone. Deformation temperatures ranging from approximately 280 ºC to 700 ºC were derived from synkinematic mineral assemblages. Temperature conditions for the zones characterized by different dynamic recrystallization mechanisms were inferred: The BLG was dominant between 280 ºC and 400 ºC, the SGR in the 400-500 ºC interval and the GBM occurred over 500 ºC.

Dynamic recrystallization microstructures of quartz can be correlated between nature and experiments. The quartz recrystallization microstructures from the eastern Tonale mylonites have been correlated with the experimental dislocation creep regimes of Hirth & Tullis (1992). For the Tonale mylonites, temperature, stress, and strain rate have been inferred, using the theoretical recrystallized grain size piezometer for recrystallization mechanisms and quartzite flow laws. Moreover, natural and experimental data sets of dynamic recrystallization microstructures of quartz in dislocations creep regime can be plotted on a strain rate versus temperature diagram (Stipp et al, 2002).

The crystallographic preferred orientation (CPO) fabric types vary according to the dominant intracrystalline slip systems that were active during deformation (Lister and Paterson, 1979; Schmid and Casey, 1986). It has been considered that the slip system activity is dominantly temperature-controlled (Takeshita, 1996).

Experimental studies (e.g. Green et al. 1970; Tullis et al. 1973) indicate that there are two dominant mechanisms by which a crystallographic preferred orientation may develop. At low temperatures and high strain rates, fabrics may develop by rotation of inequant grains or by crystallographic slip within individual grains and resultant lattice rotation. Secondly, under conditions where recrystallization is dominant, fabric development may be associated with the actual recrystallization process. These experimentally detected slip systems form the essential input data for numerical simulations of crystallographic fabric development (Lister, 1977; Takeshita & Wenk 1988). An experimental study (Muto et al, 2011) was conducted at shear strains (γ) up to 5 at a temperature of 900°C, confining pressure of 1.5 GPa, and shear strain rate of 10^{-5} s^{-1}. These experimental observations indicate that (1) the prism<a> slip system is the weakest at the experimental conditions, (2) development of a Y-max CPO requires relatively fast grain boundary migration, and (3) the development of a Y-max CPO causes geometrical softening. At the experimental conditions using single crystal samples with high water contents they observed the single-crystal samples suitably oriented for either basal<a> or prism<a> slip systems are weaker than those suitably printed for prism[c] slip system.

Schmid and Casey (1986) have conducted a complete fabric analysis for naturally deformed quartzites and suggested that slip in the crystallographic <a> direction dominates over other possible slip directions. Slip on the first order prisms, the positive and negative rhombs, and the basal plane are inferred from the fabric analysis.

The observed c-axis distributions can be classified into three main types of fabric as crossed girdles, Type I crossed girdles, single girdle and Y-maxima (Fig. 6.2). The single girdle evolves from both Type I and Type II of Lister (1977). The Y maximum evolves from the Type II crossed girdles, where crossed girdles disappear and only the maximum in the Y-direction is intensified. Type I and II crossed girdle c-axis CPOs approximately show orthorhombic symmetry with respect the sample coordinates X-Y-Z, where the X, Y, and Z are maximum, intermediate and minimum principal axes of a finite strain of the samples. These CPOs showing orthorhombic symmetry are referred to as symmetric fabrics, whereas single girdles show monoclinic symmetry (180° rotation symmetry about the Y-axis).

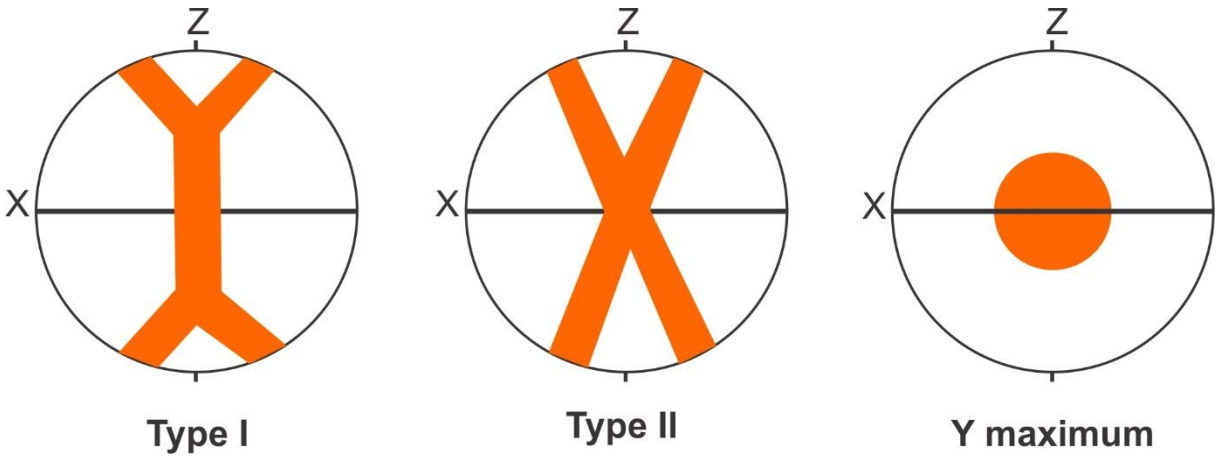

Figure 6.1. Some CPOs pattern of quartz. X, Y and Z are maximum, intermediate and minimum principal axes of finite strain (Modified from Schmid and Casey, 1986)

At temperatures above ~650°C, prism<c> becomes the dominant slip system in quartz (Mainprice et al. 1986; Law 1990) leading to an X-maximum, at upper greenschist- to amphibolite-facies conditions (450~550°C), prism<a> slip dominates leading to a Y-maximum, and under greenschist conditions (300~400°C) mixed<a> slip (prism-, rhomb-, and basal<a> slip) leading to a Type I crossed girdle pattern (Takeshita et al. 1999; Little et al. 2013).

In this study, In Area A, since protomylonite samples dominantly show Y-maximum quartz c-axis CPOs (Fig. 5.13), which formed by the dominant activation of the prism<a> slip system, the deformation temperatures are inferred to be ~400°C–550°C (Schmid and Casey 1986; Takeshita, 1996). This estimate is further constrained by the observation of subgrain formation by SGR and a core and mantle structure (e.g. sample 15112002, 15112004, 15111608; Figs. 5.2 c-d, e), suggesting the temperature conditions between ~400°C and 500°C (Stipp et al. 2002). These microstructures are

similar to those of regimes 2 described by Hirth and Tullis (1992) in experimentally deformed quartzites. In some samples, quartz c-axis CPOs show type-I crossed girdles (Schmid and Casey 1986) with R-maxima (Fig. 5.13) formed by mixed<a> slip (rhomb<a> and basal<a> slip), and hence deformation temperatures are inferred to be 300~400°C (Takeshita et al. 1999; Little et al. 2013). Further, the grain boundary bulge (Fig. 5.2e) was created by the BLG recrystallization at temperatures between ~300°C and 400°C (Shigemastsu, 1999; Stipp et al., 2002). These microstructures are similar to those of regimes 1 to 2 described by Hirth and Tullis (1992) in experimentally deformed quartzites.

In Area B, since the quartz CPOs with [c]-axes clustered parallel to the Y structural direction (Y-maximum) are dominant (Fig. 5.14), formed by the dominant activation of the prism<a> slip system, deformation temperatures are inferred to be 400°C–550°C (e.g. Schmid and Casey 1986; Takeshita, 1996). However, since some samples in the S-type mylonite zone also show a transitional fabric between the Y-maximum and type-I crossed girdles (Fig. 5.14) formed by the mixed<a> slip (prism-, rhomb-, and basal<a> slip), deformation temperatures are inferred to be 300-400 °C (e.g., Takeshita et al. 1999; Little et al. 2013). The quartz microstructure shows a large variation in mylonite zones in area B. In the mylonite zone showing P-type quartz microstructure, recrystallized quartz grains show lobate grain boundaries with large amplitude sutures (Figs. 5.3e, f and Figs. 5.23b, d) which were created by the GBM recrystallization (Poirier and Guillope, 1979) at temperatures between 500°C and 700°C (Stipp et al. 2002). Note however that the estimated temperatures could be higher in the Tonale fault zone by Stipp et al. (2002) than those in the MTL, perhaps because the strain rate could be higher in the former than the latter area. While in the mylonite showing S-type quartz microstructure core-mantle structures are developed in the deformed and recrystallized quartz grains (Figs. 5.3b, d) which was formed by the SGR recrystallization at deformation temperature between 400°C and 500°C (Stipp et al. 2002). Also, the estimated temperatures for SGR recrystallization (350–450°C) is slightly lower than the ones by Stipp et al. (2002), 400 to 500 °C, perhaps because the strain rate could be higher in the former than the latter area. At TEM scale, subgrain boundaries are often observed in the recrystallized quartz grains (Figs. 5.21, 5.22, 5.23), and free dislocation density of the recrystallized grains is the same as that of the original grains from which they were formed, which is evidenced by TEM observations, indicating that SGR recrystallization is dominant in the quartz. In some recrystallized quartz grains, curved grain boundaries occur (Fig. 5.21d) and some of them are bulged

(Fig. 5.21e) which were created by BLG recrystallization at temperatures between 300°C and 400°C (Shigemastsu, 1999; Stipp et al., 2002).

In Area B, a perthite with tapering 'flame-shaped' albite lamellae is present in some K-feldspar (Fig. 5.16a), especially at high-stress sites of S-type mylonite microstructure (Passchier 1982a). Myrmekite occurs around K-feldspar porphyroclasts (Fig. 5.16b). Myrmekite only occurs in those mylonites deformed under upper greenschist facies or amphibolite facies (Fitz Gerald & Stünitz 1993). The transition from brittle to ductile deformation of K-feldspar porphyroclast (Fig. 5.17b) occurs in mylonites consisting of recrystallized quartz grains with S-type to P-type quartz microstructure (Fig. 5.17c, d). The fact supports that the deformation temperatures in mylonite showing P-type quartz microstructure (>500 ºC) are higher than those in mylonite showing S-type one (~400 ºC; Tullis and Yund, 1987). Furthermore, based on two-feldspar geothermometry, the inferred temperatures for mylonites showing S-type quartz microstructure (350–450°C) are lower than those for mylonites showing P-type quartz microstructure (420–520°C) (Fig. 5.18; Passchier 1982a).

6.2. Differential stress and strain rate

The differential stress during steady state dislocation creep can be inferred from microstructural features (e.g. Poirier, 1985). Paleopiezometers based on recrystallized grain size and free dislocation density have been formulated and widely applied to natural rocks (e.g. Twiss, 1977; Christie and Ord, 1980; Ord and Christie, 1984) if the steady state microstructures are not significantly modified during the later geological history. The stresses that can be inferred from the paleopiezometers are reliable if the incremental strain during progressive development of the respective microstructures is sufficiently high to reach a near-steady state. In this case, the paleopiezometers may provide an estimate of the flow stress at each respective stage. Then, the preservation potential during subsequent modification by recovery, recrystallization and grain growth are discussed.

Relationships between flow stress and recrystallized grain size for quartzites in mylonite samples have been proposed by Twiss (1977). The relation proposed by Twiss (1977) has the form:

$$\sigma = A \times D^{-m} \qquad (6.1)$$

where σ denotes the differential stress (MPa), A = 603 (MPa μm^m, m = 0.68, and D is the recrystallized grain size (μm).

Then, Stipp and Tullis (2003) based on experimental results of deformed Black Hills quartzite derived the recrystallized grain size piezometer for quartz as:

$$D = 10^{3.56 \pm 0.27} \times \sigma^{-1.26 \pm 0.13} \quad (6.2)$$

The recrystallized grain size piezometer for quartz, which is calibrated for use with EBSD data, is as follows by Cross et al. (2017).

$$D = 10^{3.91 \pm 0.41} \times \sigma^{-1.41 \pm 0.21} \quad (6.3)$$

In this study, I use the piezometer of Cross et al. (2017) to constrain the differential stress during deformation of samples deformed by dislocation creep under steady state (Table 5.1).

The relationship between the free dislocation density in quartz and the flow stress is given by the relation:

$$\sigma = C \text{ x } \rho^p \quad (6.4)$$

where σ is the steady-state differential stress in MPa; ρ is the dislocation density in cm^{-2}. $C = 1.64 \text{ x } 10^{-4}$, and $p = 0.66$ (McCormick, 1977; Ord and Christie, 1984). Flow stresses (MPa) which are calculated from dislocation densities are shown in table 5.4.

Fig. 6.2 shows the differential stresses in proto-mylonite and mylonite from the MTL that are estimated by recrystallized grain size piezometer and free dislocation density piezometer. In Area A, stress estimated by recrystallized grain size piezometer for proto-mylonite are between 80 and 250 MPa while stress estimated by free dislocation density piezometer is lower being between 55 and 102 MPa. Suggesting high-stress prevailed in Area A, followed by recovery and static recrystallization shown by lower differential stress inferred from the dislocation densities.

In Area B, stress about 100 MPa is inferred from recrystallized grain size piezometer, which is similar to those inferred from free dislocation density piezometer in S-type mylonite microstructure. P-type mylonite microstructure, stress estimated by recrystallized grain size piezometer are between 20 and 40 MPa, while stress estimated by free dislocation density piezometer is higher between 40 and 90 MPa. The higher stress that is estimated by free dislocation density piezometer could indicate a small amount of overprinting deformation at higher stress.

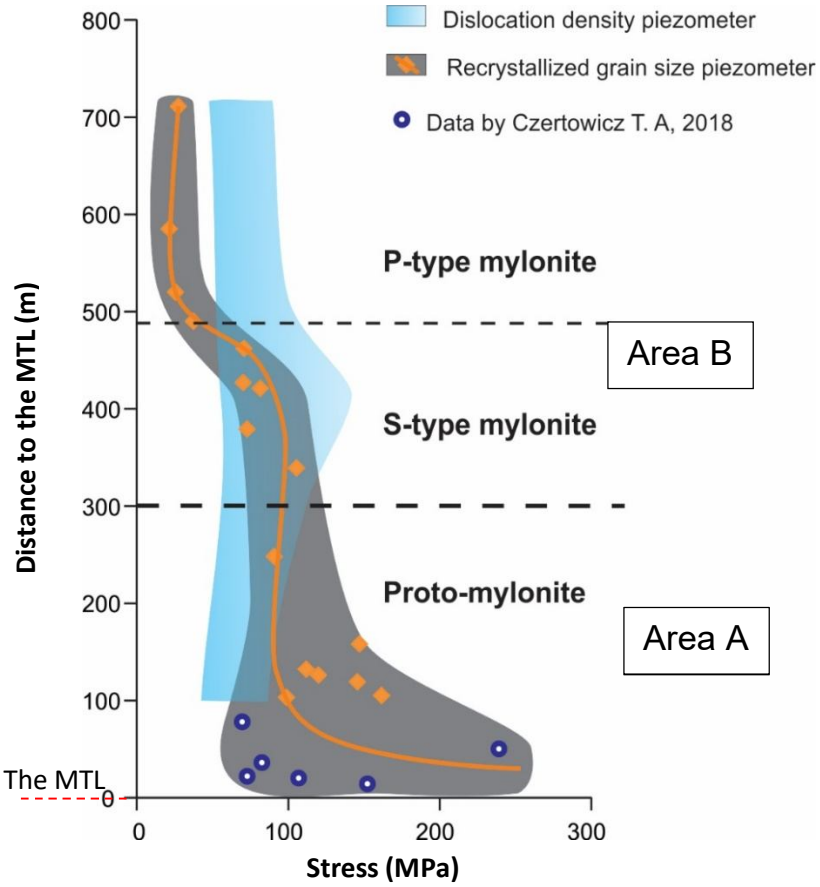

Figure 6.2. Differential stress in protomylonite and mylonite from the MTL estimated by recrystallized grain size piezometer and free dislocation density piezometer.

To constrain the stresses and strain rates in the mylonites, I analyze flow stress–grain size maps for dislocation creep for a quartz aggregate. Dislocation creep is represented by the flow law proposed by Gleason et al (1995):

$$\dot{\varepsilon} = A\,\sigma^{n}\,e^{(-E/RT)} \tag{6.5}$$

where $\dot{\varepsilon}$ is the strain rate (s^{-1}), A is a material constant = 1.1 x 10^{-4} ($MPa^{-n}s^{-1}$), σ is differential stress (MPa), n is the stress exponent (4), E is the activation energy (223 $kJmol^{-1}$), R is the universal gas constant (8.314 $Jmol^{-1}K^{-1}$), and T is temperature (K).

Based on the equation (6.5), I calculated the strain rate for the quartz aggregates for the inferred differential stresses from the recrystallized grain size of quartz at temperatures of 400 °C and 500 °C (Fig. 6.3). At the same stress level, strain rate at high temperature is higher than that at low temperature. I estimate that strain rate for the proto-mylonites was ~10^{-15} s^{-1} at 400 °C, that for the S-type mylonite microstructure was and 10^{-16} s^{-1} for 400 °C, and that for the P-type mylonite microstructure was 10^{-16} s^{-1} for 500 °C.

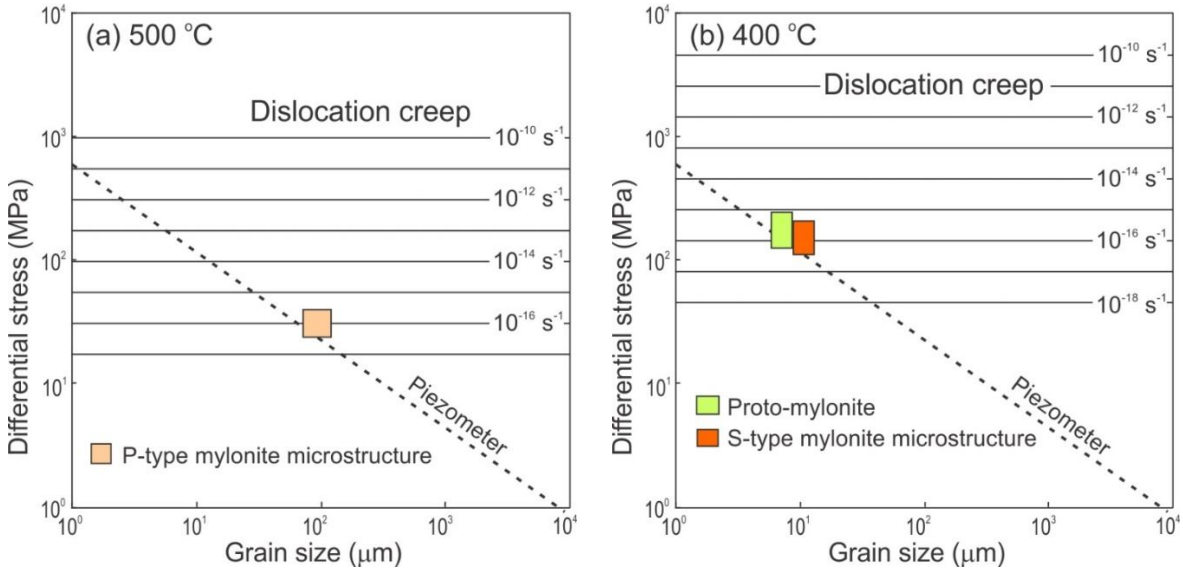

Figure 6.3. Plotting of flow stress versus grain size for a quartz aggregate at 500 °C and 400 °C for strain rates of 10^{-18} to 10^{-10} s^{-1}

6.3. Overprinting and strain localization

The S-type mylonite in Area B, which occurred at the positions of 300 m to 490 m far from the MTL in the northern side (Fig.5.1), consists of K-feldspar porphyroclast, plagioclase, strongly deformed quartz ribbon grains (Fig. 3.2b; Fig. 3.3b; Fig. 3.4) and strongly foliated. The coarse and strongly flattened ribbon quartz grains with undulose extinction (Fig. 5.3a), which show a high aspect ratio (R~10) aligned nearly parallel to the foliation (e.g. Samples 171101001; Fig. 6.4), are surrounded by fine equant grains (core-mantle structures (Fig. 5.3b, d) (Guillope and Poirier, 1979; White, 1976). On the other hand, the aspect ratio in of quartz grains in samples from proto-mylonite and P-type mylonite microstructure were less than 6 and also the orientation of the long-axis is fairly scattered, indicating that high strain occurred in the S-type mylonite microstructure zone.

The calculation the GOS threshold following Cross et al. (2017) to separate recrystallized and relict quartz grains shows that in S-type mylonite the GSO threshold is ~5° (Fig. 6.4) is higher than the ones of proto-mylonite (~3 °) and P-type mylonite (2-4 °) (Fig 6.4). The GOS gives the misorientation angle between every pixel in a grain and the mean orientation of that grain, which can be analyzed by EBSD data. The misorientation was formed by intracrystalline lattice distortion caused by subgrain rotation (i.e. polygonization). The higher GOS threshold of quartz recrystallized grains in S-type mylonite could indicate that the strain rate is higher than the rate of recovery

and/or recrystallization. The observed dislocation substructure in quartz grain using the TEM from S-type mylonite samples shows that free dislocation density is very high ($1x10^8$ cm^{-2} and $14x10^8$ cm^{-2}) (Fig. 5.24 c) and a numerous dislocation tangle (Fig. 5.21), conforming to the high GOS value.

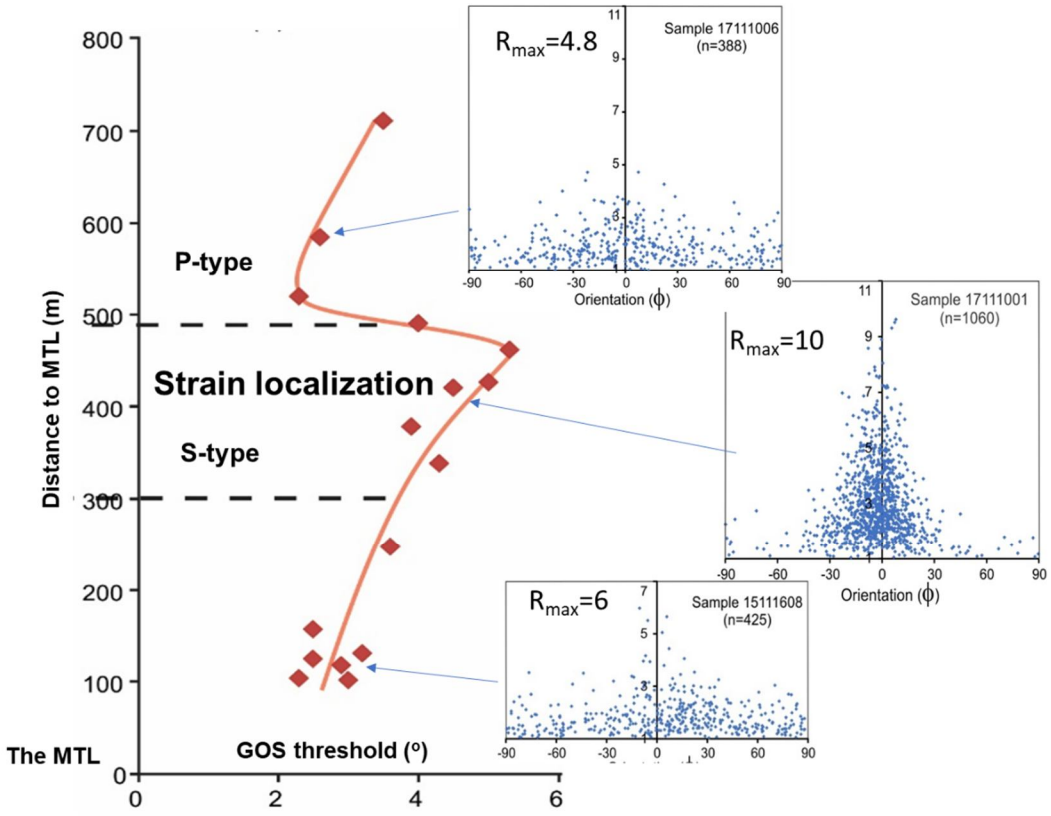

Figure 6.4. Zone of high GOS values as a result of strain localization in the S-type mylonite corresponding to high aspect ratio.

Changes in temperature conditions during the progression of strain localization can be also evidenced by the change in recrystallization mechanism. In the zone showing P-type quartz microstructure, grain-boundary migration (GBM) recrystallization occurred at higher-temperature conditions than those where S-type microstructures (Figs. 5.3a, b, d) form by subgrain-rotation (SGR) recrystallization (Guillope and Poirier, 1979; White, 1976; Hirth and Tullis, 1992; Stipp et al., 2002). Furthermore, detailed observations of dislocation substructures of quartz showing S-type microstructure by the TEM show that grain boundaries of quartz are curved and bulged (Fig. 5.21e, f) suggesting that they form by the process of the BLG. The occurrence of different sizes of recrystallized quartz grains in the same sample indicates that overprinting occurred in the recrystallized quartz grains showing S-type microstructures. The large quartz recrystallized grains (c. 70 µm) were overprinted by

the SGR and the BLG recrystallization which created the small recrystallized grain sizes varying between 11.4–20 μm (Table 5.1; Fig 5.16a).

The present study, therefore, provides a general trend of microstructural development with progressive deformation in the MTL shear zone (Fig. 6.6). Initially, the granite rock and tonalite rock formed in the northern part of the MTL (Fig. 6.6a) in the Late Cretaceous (Ichikawa, 1980; Shimada et al., 1998). During the Late Cretaceous, left-lateral strike-slip motion occurred along the proto-MTL (i.e. southern marginal shear zone, e.g. Sakakibara, 1995; Shimada et al., 1998), the deformation history of which can be divided into several stages under various stress fields and strain rate during exhumation.

In summary, the deformation of the southern marginal shear zone started to occur at a temperature of approximately 500 ºC in Area B (Fig. 6.6b) where granite rock was deformed into the P-type mylonite. At this deformation temperature, quartz grains with P-type microstructure show a smaller aspect ratio, less developed undulatory extinction, and lobate grain boundaries with large amplitude sutures which were created by the GBM recrystallization. The CPO of quartz aggregates from P-type shows a Y maximum pattern. An elongated and fish shape of K-felspar grain was observed in the P-type mylonite zone, showing higher deformation temperatures than 450 ºC.

At the temperature of approximately 450 ºC, the deformation stopped in the northern part of P-type based on the results of two feldspar geothermometry, the southern part continues to deform forming P-type mylonite in Area B (Fig. 6.6c). While in Area A, the tonalite rock was deformed into proto-mylonite. At this deformation temperature, the proto-mylonite is less deformed than P-type mylonite, so that some of the original igneous quartz grains are preserved, although they occur as highly flattened relict grains, showing patchy and undulose extinction, and deformation lamellae (Fig. 5.2a). These relict quartz grains are surrounded by equigranular aggregates of recrystallized small quartz grains that form by the process of the SGR (Guillope and Poirier, 1979; White, 1976; Hirth and Tullis, 1992; Stipp et al., 2002). The CPO of quartz aggregates from both P-type and proto-mylonite show a Y maximum pattern.

At the temperature of approximately 400 ºC (Fig. 6.6d), the deformation stopped in the northern part of part of granitic mylonite zone in Area B where P-type mylonite zone extends from 490 m to 800 m towards the north from the MTL. In the southern part of granitic mylonite zone in Area B, which extends from 300 m to 490 m towards the north from the MTL, continues to deform forming S-type microstructures in

deformed and recrystallized quartz with high aspect ratio. The CPO of quartz shows a transitional fabric between the Y-maximum and type-I crossed girdles. Broken K-feldspar porphyroclasts was observed, showing deformation temperatures less than 450 ºC. The strain localization occurred in the narrow zone. In Area A, the protomylonite, where recrystallized grains also show S-type microstructure and somewhat smaller recrystallized grain size (c. 10 μm), deformed at similar conditions, but slightly higher stress conditions.

At the temperature of approximately 350 ºC (Fig. 6.6e) the deformation stopped in Area A and the northern part of S-type mylonite microstructure zone, and only the southern part (300-350 m) continues to deform at 350 ºC forming S-type microstructures in deformed and recrystallized quartz. In this S-type mylonite microstructure, the large recrystallized quartz grains were overprinted by small recrystallized quartz grains by the BLG.

At the temperature 300-350 ºC (Fig. 6.6f) the plastic deformation was stopped in Area B, and the further plastic deformation only occurred in the narrow zone less than 50 m thick along the MTL, forming ultramylonite at temperature conditions of 300 ºC (Czertowicz et al., in review). In the ultramylonite, type I crossed girdle with R-maxima formed in the quartz aggregates constituting the ultramylonite, but later the c-axis fabric becomes randomized in the ultramylonite accompanied by the formation of abundant white mica.

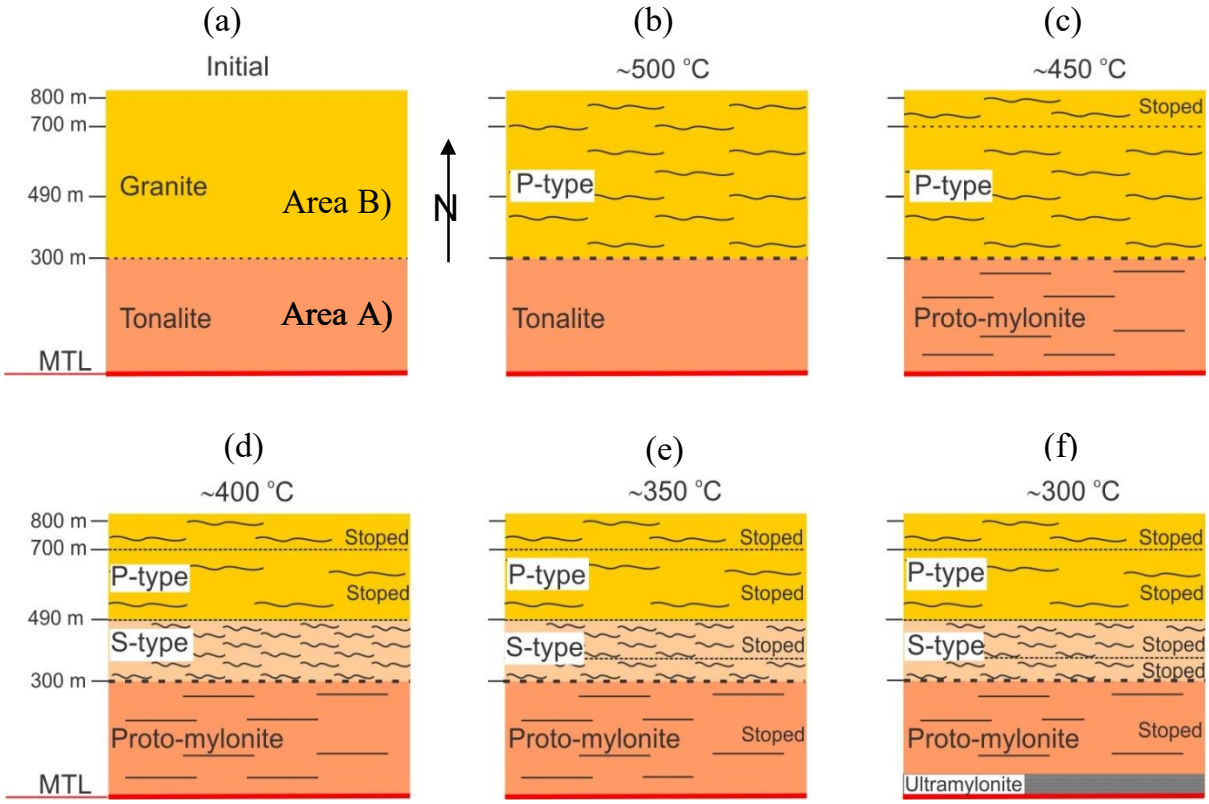

Figure 6.6. The development of microstructure in the MTL shear zone during cooling. (a) Initially, the granite rock (Area A) and tonalite rock (Area B) formed in northern part of the MTL. (b) the deformation started to occur at temperature approximately 500 °C granite rock was deformed into P-type mylonite in Area B. (c) the deformation stopped in the northern part of P-type at temperature of approximately 450 °C, the southern part continues to deform forming P-type mylonite in Area B while the tonalite rock was started to deform into proto-mylonite in Area A. (d) the deformation stopped in the proto-mylonite zone and in the P-type zone at temperature approximately 400 °C, only in the southern part of granitic mylonite zone in Area B continues to deform forming S-type microstructures. (e) the deformation stopped in the northern part of S-type mylonite microstructure zone, and only the southern part continues to deform at 350 °C. (f) the plastic deformation was stopped in Area B, and the further plastic deformation only occurred in the narrow zone less than 50 m thick along the MTL.

7. Conclusions

In this study, the following conclusions have been drawn based on field geological observations and analytical work in laboratories.

(1) The mylonitic rocks derived from the Ryoke granitoids in the northern area from the MTL, along the Akaiwadani-River consist of two types of mylonitic rocks distributed in different areas. Area A mostly consists of protomylonite, which originated from tonalite, up to c. 300 m wide from the MTL, and Area B, the area further north which is up to c. 500 m wide, consists of mylonite, which originated from granite. The asymmetric K-feldspar porphyroclasts (σ texture) and the S/C texture that commonly developed in mylonites indicate the sinistral sense of shear (i.e. north wall to the west) that occurred in the Kashio phase during the Late Cretaceous.

(2) In protomylonite from the area A, some highly flattened relict quartz grains, showing patchy and undulose extinction, and deformation lamellae occur, which are surrounded by equigranularity aggregates of recrystallized small quartz grains (core and mantle structure) formed by the process of subgrain rotation recrystallization. In recrystallized quartz from some other samples, grain boundaries bulge into the crystal with high dislocation density, forming new small crystals by bulging recrystallization. The aspect ratio of the recrystallized quartz grains is less than 6, and the preferred orientation of the long axis is weak. The mean recrystallized grains size of quartz for protomylonite samples in the Area A are a range of 6 μm to 15 μm.

(3) Mylonites in Area B consists of two types of the microstructure of quartz: S-type mylonite and P-type. The S-type mylonite, which occurred at the positions of 300 m to 490 m northward distance from the MTL, consists of coarse strongly flattened ribbon grains with a high aspect ratio (R~ 11) which are surrounded by fine equant grains (core-mantle structures). The microstructure features indicate that the SGR dynamic recrystallization occurred in the S-type mylonite. Mean recrystallized grain sizes of quartz vary between 11.4–20 μm. The P-type mylonite occurred at the positions of 480 m to 800 m northward distance from the MTL where recrystallized quartz grains show a smaller aspect ratio, less developed undulatory extinction, and lobate grain boundaries with large amplitude sutures which were created by the GBM recrystallization. The recrystallized grain size of quartz varies between c. 100-120 μm.

(4) The quartz CPOs with [c]-axes clustered parallel to the Y structural direction (Y-maximum) dominate in both areas A and B. However, some samples in the proto-mylonite show a type-I crossed girdle quartz c-axis fabric with R-maxima, and in some of the S-type mylonite a transitional quartz c-axis fabric between the Y-maximum and type-I crossed girdles occurs.

(5) K-feldspar is abundant and strongly deformed in P-type mylonite of Area B with dominant intergrowth of myrmekite. In S-type mylonite, K-feldspar porphyroclasts show brittle deformation, whereas P-type mylonite, K-feldspar porphyroclasts show ductile deformation with an elongated ribbon or fish shape.

(6) Variable deformation conditions occurred within the MTL shear zone. The deformation of quartz occurred at high temperatures around 500 ^{o}C in the wide zone forming P-type quartz microstructures in Area B and proto-mylonite in Area A. However, the strain was localized during cooling of the granitic mylonites in Area B, and in S-type microstructures zone, ductile deformation of quartz continues to occur at 350 to 400 ^{o}C, forming smaller recrystallized quartz. The strain localization occurred at different stress of ~100 MPa and strain rate of 10^{-16} s^{-1} at temperature conditions of c. 400 ^{o}C. This difference in deformation temperature conditions resulted in the variation in not only the quartz microstructure but also the quartz CPO patterns and K-feldspar microstructure.

References

Allmendinger, 1988. STEREONET; a plotting program for orientation data Computer program + manual, p. 30.

Ando J, Fujino K, Takeshita T, 1993. Dislocation microstructures in naturally deformed silicate garnets. Phys Earth Planet Inter 80:105–116. doi:10.1016/0031-9201(93)90041-7

Christie, J.M. and Ord, A., 1980. Flow stress from microstructures of mylonites: example and current assessment. J. Geophys. Res., 85: 6253-6262.

Cross AJ, Prior DJ, Stipp M, Kidder S, 2017. The Recrystallized Grain Size Piezometer for Quartz: An EBSD-based calibration. Geophys Res Lett 44:6667–6674.

Drury, M. R., Humphreys, F. J. & White, S. H., 1985. Large strain deformation studies using polycrystalline magnesium as a rock analogue. Part 1I: dynamic recrystallisation mechanisms at high temperatures. Physics of the Earth and Planetary Interiors, 40, 208-222.

Famin V, Raimbourg H, Garcia S, Bellahsen N, Hamada Y, Boullier A-M, Fabbri O, Michon L, Uchide T, Ricci T, Hirono T, Kawabata K, 2014. Stress rotations and the long-term weakness of the Median Tectonic Line and the Rokko-Awaji Segment. Tectonics 33. http://dx.doi.org/10.1002/2014TC003600.

Fitz Gerald J. D. & Stünitz H. 1993. Deformation of granitoids at low metamorphic grade. I: Reactions and grain size reduction. Tectonophysics 221, 269–97.

Fukunari T, Wallis SR, 2007. Structural evidence for large-scale top-to-the-north normal displacement along the Median Tectonic Line in southwest Japan. Isl Arc 16:243–261.

Ghosh S.K, 1993. Structural Geology: Fundamentals and Modern Developments Pergamon Press, Oxford 598 pp.

Gleason GC, Tullis J, 1995. A flow law for dislocation creep of quartz aggregates determined with the molten salt cell. Tectonophysics 247:1–23

Green, H. W., D. T. Griggs, and J. M. Christie, 1970. Syntectonlc and annealing recrystalllzatlon of finegrained quartz aggregates, in Experimental and Natural Rock Deformation, edited by W. Paulitsch, pp. 272-335, Springer-Verlag, Heidelberg.

Guillope, M., Poirier, J.P., 1979. Dynamic recrystallisation during creep of single crystalline halite: an experimental study. Journal of Geophysical Research 84, 5557e5567.

Haakon Fossen, Geane Carolina G. Cavalcante, Shear zones – A review, Earth-Science Reviews, Volume 171, 2017, Pages 434-455, ISSN 0012-8252, https://doi.org/10.1016/j.earscirev.2017.05.002.

Hara I, Shyoji K, Sakurai Y, et al, 1980. Origin of the Median Tectonic Line and its initial shape. Mem Geol Soc Japan 18:27–49.

Hirth, G., Tullis, J., 1992. Dislocation creep regimes in quartz aggregates. Journal of Structural Geology 14, 145e159.

Hobbs, B. E., 1968. Recrystallization of single crystals of quartz. Tectonophysics, 6, 353-401.

Huzita K, 1980. Role of the Median Tectonic Line in the Quaternary tectonics of the Japanese islands. Mem Geol Soc Japan 18:129–153.

Ichikawa K, 1980. Geohistory of the Median Tectonic Line of Southwest Japan. J Geol Soc Japan 18:187–212.

Ito, M., 1978. Granitic rocks and mylonitisation m the Kayumi district Mie Prefecture. MTL 3, 99-101

Ito T, Ikawa T, Yamakita S, Maeda T, 1996. Gently north-dipping Median Tectonic Line (MTL) revealed by recent seismic reflection studies, southwest Japan. Tectonophysics 264:51–63.

Ito T, Kojima Y, Kodaira S, et al, 2009. Crustal structure of southwest Japan, revealed by the integrated seismic experiment Southwest Japan 2002. Tectonophysics 472:124–134.

Jefferies SP, Holdsworth RE, Shimamoto T, et al, 2006a. Origin and mechanical significance of foliated cataclastic rocks in the cores of crustal-scale faults: Examples from the Median Tectonic Line, Japan. J Geophys Res 111:B12303.

Jefferies SP, Holdsworth RE, Wibberley CAJ, et al, 2006b. The nature and importance of phyllonite development in crustal-scale fault cores: An example from the Median Tectonic Line, Japan. J Struct Geol 28:220–235.

Kubota Y, Takeshita T, 2008. Paleocene large-scale normal faulting along the Median

Tectonic Line, western Shikoku, Japan. Isl Arc 17:129–151.

Law RD., 1990. Crystallographic fabrics: a selective review of their applications to research in structural geology. Geol Soc London, Spec Publ 54:335–352.

Lister G.S, 1977. Crossed-girdle c-axis fabrics in quartzites plastically deformed by plane strain and progressive simple shear.

Lister, G. S. 1978. Discussion: Crossed girdle c-axis fabrics in quartzites plastically deformed by plane strain and progressive simple shear. Tectonophysics, 39, 51-54.

Lister G S , Paterson M S, 1979. The simulation of fabric development during plastic deformation and its application to quartzite: fabric transitions. Journal of Structural Geology 1 (2), 99e115.

Little TA, Hacker BR, Brownlee SJ, Seward G., 2013. Microstructures and quartz lattice-preferred orientations in the eclogite-bearing migmatitic gneisses of the D'Entrecasteaux Islands, Papua New Guinea. Geochemistry, Geophys Geosystems 14:2030–2062.

Mainprice D, Bouchez J-L, Blumenfeld P, Tubía JM, 1986. Dominant c slip in naturally deformed quartz: Implications for dramatic plastic softening at high temperature. Geology 14:819–822.

Masuda T, Fujimura A, 1981. Microstructural development of fine-grained quartz aggregates by syntectonic recrystallization. Tectonophysics, 72, pp. 105-128.

McCormick J W, 1977. Transmission electron microscopy of experimentally deformed synthetic quartz. PhD thesis, University of California.

McLaren A C & Hobbs B E, 1972. Transmission electron microscope investigation of some naturally deformed quartzites. In: Flow and fracture of rocks (edited by Heard, H. C., Borg, I. Y., Carter, N. L. & Raleigh, C. B.) 16. Geophysical Monograph, 55-66

McLaren A C, 1991. Transmission electron microscopy of minerals and rocks. Cambridge topics in mineral physics and chemistry: Cambridge, Cambridge University Press.

Miyata T, 1990. Slump strain indicative of paleoslope in Cretaceous Izumi sedimentary basin along Median tectonic line, southwest Japan. Geology 18:392–394.

Mori H, Wallis S, Fujimoto K, Shigematsu N, 2015. Recognition of shear heating on a long-lived major fault using Raman carbonaceous material thermometry: Implications for strength and displacement history of the MTL, SW Japan. Isl Arc 24:425–446.

Muto, J., G. Hirth, R. Heilbronner, and J. Tullis, 2011. Plastic anisotropy and fabric evolution in sheared and recrystallized quartz single crystals, J. Geophys. Res., 116, B02206, doi:10.1029/2010JB007891

Noda A, Danhara T, Iwano H, Hirata T, 2017. LA-ICP-MS U-Pb and fission-track ages of felsic tuff beds of the Takikubo Formation, Izumi Group in the Kan-onji district, eastern Shikoku, southwestern Japan. Bull Geol Surv Japan 68:119–130.

Ohira, Y, 1982. Geology of the Ryoke belt in the northern area of Mt. Takami, central Kii Peninsula, Japan. Journal of Geological Society of Japan, 88, 467-481.

Ohtomo, Y., 1993. Origin of the Median Tectonic Line. Journal of Science of the Hiroshima University 9, 611-669.

Okada, A., 1980. Quaternary faulting along the Median Tectonic Line of Southwest Japan. Mem. Geol. Geol. Soc. Jpn. 18, 79–108.

Okada A, 2012. Research on Quaternary faulting history and long-term seismic evaluation of the Median Tectonic Line (MTL) fault zone in southwest Japan. Quat Res 51:131–150.

Okudaira T, Beppu Y, Yano R, et al, 2009. Mid-crustal horizontal shear zone in the forearc region of the mid-Cretaceous SW Japan arc, inferred from strain analysis of rocks within the Ryoke metamorphic belt. J Asian Earth Sci 35:34–44.

Okudaira T, Shigematsu N, 2012. Estimates of stress and strain rate in mylonites based on the boundary between the fields of grain-size sensitive and insensitive creep. J Geophys Res 117: B03210.

Ord A, Christie J M, 1984. Flow stresses from microstructures in mylonitic quartzites of the Moine Thrust zone, Assynt area, Scotland. J. Struct. Geol. 6: 639-654.

Poirier J. P. 1985. Creep of Crystals: High temperature Deformation Processes in Metals. Ceramics and Minerals. Cambridge University Press, Cambridge

Passchier CW, 1982a. Mylonitic deformation in the Saint-Barthélemy Massif, French Pyrenees, with emphasis on the genetic relationship between ultramylonite and

pseudotachylyte. GUA Pap Geol Ser 1 16:1–173.

Passchier CW, Trouw RAJ, 1998. Microtectonics. Springer-Verlag Berlin Heidelberg, New York

Sakakibara, N., Ohtomo, Y., Hara, 1., 1989. Deformation of granitic rocks in the Ryoke belt (I) Deformation styles of quartz. DELP publication 28, 47-51.

Sakakibara, N., 1995, Structural evolution of multiple ductile shear zone system in the Ryoke belt, Kinki Province. Journal of Science, Hiroshima University, Series C, 10, 267-332.

Sakakibara N, 1996. Qualitative estimation of deformation temperature and strain rate from microstructure and lattice preferred orientation in plastically deformed quartz aggregates. J Geol Soc Japan 102:199–210.

Sakashima T, Terada K, Takeshita T, Sano Y, 2003. Large-scale displacement along the Median Tectonic Line, Japan: evidence from SHRIMP zircon U–Pb dating of granites and gneisses from the South Kitakami and paleo-Ryoke belts. J Asian Earth Sci 21:1019–1039.

Sakashima T, Terada K, Takeshita T, Sano Y, 2003. Large-scale displacement along the Median Tectonic Line, Japan: evidence from SHRIMP zircon U–Pb dating of granites and gneisses from the South Kitakami and paleo-Ryoke belts. J Asian Earth Sci. 21:1019–1039.

Schmid SM, Casey M, 1986. Complete fabric analysis of some commonly observed quartz c-axis fabrics. Miner Rock Deform Lab Stud 36:263–286.

Shigematsu N. 1999. Dynamic recrystallization in deformed plagioclase during progressive shear deformation. Tectonophysics 305, 437–52

Shigematsu N, Fujimoto K, Tanaka N, et al, 2012. Internal structure of the Median Tectonic Line fault zone, SW Japan, revealed by borehole analysis. Tectonophysics 532–535:103–118.

Shigematsu N, Kametaka M, Inada N, Miyawaki M, Miyakawa A, Kameda J, Togo T, Fujimoto K, 2017. Evolution of the Median Tectonic Line fault zone, SW Japan, during exhumation, Tectonophysics, Volumes 696–697, Pages 52-69, ISSN 0040-1951, https://doi.org/10.1016/j.tecto.2016.12.017.

Shimada, K., Takagi, H., Osawa, H., 1998. Geotectonic evolution in transpressional

regime: time and space relationships between mylonitization and folding in the southern Ryoke belt, eastern Kii Penisular, southwest Japan. J. Geol. Soc. Jpn. 104, 825–844 (in Japanese with English abstract).

Sibson RH, 1977. Fault rocks and fault mechanisms. J Geol Soc London 133:191–213.

Simpon C. 1985. Deformation of granitic rocks across the brittle-ductile transition. Journal of Structural Geology 7, 503–11.

Simpon C & wintsch R P, 1989. Evidence for deformation-induced K-feldspar replacement by myrmekite. Journal of Metamorphic Geology 7, 261–75.

Stipp, M., H. Stu¨nitz, R. Heilbronner, and S. M. Schmid, 2002a. Dynamic recrystallization of quartz: Correlation between natural and experimental conditions, Geol. Soc. Spec. Publ. London, 200, 171–190, edited by S. De Meer, M. R. Drury, J. H. P. De Bresser, and G. M. Pennock.

Stipp, M., H. Stu¨nitz, R. Heilbronner, and S. M. Schmid, 2002b. The eastern Tonale fault zone: A ‘‘natural laboratory’’ for crystal plastic deformation of quartz over a temperature range from 250C to 700C, J. Struct. Geol., 24, 1861– 1884.

Stipp, M., and J. Tullis, 2003. The recrystallized grain size piezometer for quartz, Geophys. Res. Lett., 30(21), 2088, doi:10.1029/2003GL018444

Stormer, J.C., 1975. A practical two-feldspar geothermometer. American Mineralogist, 60: 667-674-7.

Stormer, J.C. and Whitney, J.A., 1977. Two-feldspar geothermometry in granulite facies metamorphic rocks. Contrib. Mineral. Petrol., 65: 123-133.

Streckeisen A, 1976. To each plutonic rock its proper name, Earth-Science Reviews, Volume 12, Issue 1, Pages 1-33, ISSN 0012-8252.

Takagi H, 1986. Implications of mylonitic microstructures for the geotectonic evolution of the Median Tectonic Line, central Japan. J Struct Geol 8:3–14.

Takagi H, Takeshita T, Shibata K, et al, 1992. Middle Miocene normal faulting along the Tobe Thrust in setern Shikoku. J Geol Soc Japan 98:1069–1072.

Takagi H, Takahashi K, Shimada K, et al, 2012. Integrated estimates of the thickness of the fault damage zone in granitic terrain based on penetrative mesocracks and XRD analyses of quartz. J Struct Geol 35:64–77.

Takasu A, Dallmeyer RD, 1990. $^{40}Ar/^{39}Ar$ mineral age constraints for the tectonothermal evolution of the Sambagawa metamorphic belt, central Shikoku, Japan: a Cretaceous accretionary prism. Tectonophysics 185:111–139.

Takeshita T and Wenk H-R, 1988. Plastic anisotropy and geometrical hardening in quartzites. Tectonophysics, 149, 345-361.

Takeshita T, 1993. Deformation of the forearc region and along the Median Tectonic Line in southwest Japan during the opening of the Japan sea: A preliminary report. Mem Geol Soc Japan 42:225–244.

Takeshita, T. and Marimoto, K, 1996. Anisotropic Nd-Fe-B Bonded Magnets Made from HDDR Powders. Journal Applied Physics, 79, 5040-5044. http://dx.doi.org/10.1063/1.361567

Takeshita T, Wenk H-R, Lebensohn R, 1999. Development of preferred orientation and microstructure in sheared quartzite: comparison of natural data and simulated results. Tectonophysics 312:133–155.

Takeshita T, El-Fakharani AH, 2013. Coupled micro-faulting and pressure solution creep overprinted on quartz schist deformed by intracrystalline plasticity during exhumation of the Sambagawa metamorphic rocks, southwest Japan. J Struct Geol 46:142–157.

Tullis J., Snoke A. W. & Todd V. R, 1982. Significance and petrogenesis of mylonitic rocks. Geology 10, 227–30.

Toy VG, Prior DJ, Norris RJ (2008) Quartz fabrics in the Alpine Fault mylonites: Influence of pre-existing preferred orientations on fabric development during progressive uplift. J Struct Geol 30:602–621.

Tullis, J., J. M. Christie, and D. T. Griggs, Microstructures and preferred orientations of experimentally deformed quartzites, Bull. Geol. Soc. America, 8__4, 297-314, 1973.

Tullis J and Yund R, 1987. Transition from cataclastic flow to dislocation creep of feldspar: Mechanism and microstructures Geology, 15 (1987), pp. 606-609

Twiss R J, 1977. Theory and applicability of a recrystallized grain size paleopiezometer, Pageoph., 115, 227–244.

Urai, J. L., Mans, W. D. & Lister, G. S. 1986. Dynamic recrystallization of minerals. In:

HOBBS, B. E. & HEARD, H. C. (eds) Mineral and Rock Deformation: Laboratory Studies. Geophysical Monograph, 36, 161-199.

Vauchez, A., Tommasi, A., Mainprice, D., 2012. Faults (shear zones) in the Earth's mantle. Tectonophysics 558–559, 1–27. http://dx.doi.org/10.1016/j.tecto.2012.06.006.

Vernon R. H., Williams V. A. & Darcy W. F, 1983. Grain-size reduction and foliation development in a deformed granitoid batholith. Tectonophysics 92, 123–45.

Vernon R. H. 1992. Questions about myrmekite in deformed rocks. Journal of Structural Geology13, 979–85.

Toy VG, Prior DJ, Norris RJ., 2008. Quartz fabrics in the Alpine Fault mylonites: Influence of pre-existing preferred orientations on fabric development during progressive uplift. J Struct Geol 30:602–621.

Vollmer FW., 1990. An application of eigenvalue methods to structural domain analysis. Bull Geol Soc Am 102:786–791.

White, S. H. 1973. Syntectonic recrystallisation and texture development in quartz. Nature, 244, 276-277

White, S.H., 1976. The effects of strain on microstructures, fabrics, and deformation mechanisms in quartzites. Philosophical Transactions of the Royal Society of London A283, 69e86.

Woodcock NH., 1977. Specification of fabric shapes using an eigenvalue method. GSA Bull 88:1231–1236.

Wright S I, Nowell M M and Field D P, 2011. A Review of strain analysis using electron backscatter diffraction, Microsc. Microanal., 17(3), 316–329, doi:10.1017/S1431927611000055.